AGU PUBLICATIONS

JGR

Journal of Geophysical Research: Planets

RESEARCH ARTICLE
10.1002/2017JE005395

Special Section:
Mars Aeronomy

Field-Aligned Electrostatic Potentials Above the Martian Exobase From MGS Electron Reflectometry: Structure and Variability

Robert J. Lillis[1], J. S. Halekas[2], M. O. Fillingim[1], A. R. Poppe[1], G. Collinson[3], David A. Brain[4], and D. L. Mitchell[1]

[1]Space Sciences Laboratory, University of California Berkeley, Berkeley, CA, USA, [2]Department of Physics and Astronomy, University of Iowa, Iowa city, IA, USA, [3]NASA Goddard Space Flight Center, Greenbelt, MD, USA, [4]Laboratory for Atmospheric and Space Physics, University of Colorado, Boulder, CO, USA

Abstract Field-aligned electrostatic potentials in the Martian ionosphere play potentially important roles in maintaining current systems, driving atmospheric escape and producing aurora. The strength and polarity of the potential difference between the observation altitude and the exobase (~180 km) determine the energy dependence of electron pitch angle distributions (PADs) measured on open magnetic field lines (i.e. those connected both to the collisional atmosphere and to the interplanetary magnetic field). Here we derive and examine a data set of ~3.6 million measurements of the potential between 185 km and 400 km altitude from PADs measured by the Mars Global Surveyor Magnetometer/Electron Reflectometer experiment at 2 A.M./2 P.M. local time from May 1999 to November 2006. Potentials display significant variability, consistent with expected variable positive and negative divergences of the convection electric field in the highly variable and dynamic Martian plasma environment. However, superimposed on this variability are persistent patterns whereby potential magnitudes depend positively on crustal magnetic field strength, being close to zero where crustal fields are weak or nonexistent. Average potentials are typically positive near the center of topologically open crustal field regions where field lines are steeper, and negative near the edges of such regions where fields are shallower, near the boundaries with closed fields. This structure is less pronounced for higher solar wind pressures and (on the dayside) higher solar EUV irradiance. Its causes are uncertain at present but may be due to differential motion of electrons and ions in Mars's substantial but (compared to Earth) weak magnetic fields.

Plain Language Summary The Aurora Borealis, or northern lights, occur when high-energy electrons from space collide violently with our upper atmosphere. These electrons receive their energy from strong electric fields that accelerate them downward along the force lines of the earth's global magnetic field. On Mars, accelerated electrons are also responsible for the aurora that has been observed by both the Mars Express and MAVEN spacecraft. In this study we use the observed properties of upward- and downward-traveling electrons measured by the Mars Global Surveyor spacecraft to deduce the strength of these important electric fields. We find that they are highly variable, as is to be expected from the dynamic interaction of the solar wind (a stream of charged particles constantly ejected by the sun) with the Mars upper atmosphere. However, these electric fields also show persistent patterns in regions where Mars' crustal rocks are most strongly and coherently magnetized. Here, the electric fields are predominantly downward where the magnetic field lines are more horizontal and predominantly upward where they are more vertical. Detailed modeling and further observations will be required to fully understand the plasma dynamics behind this phenomenon.

Key Points:
- Field-aligned electrostatic potentials are derived from energy dependence of electron loss cones measured at ~400 km altitude
- Strong potentials are associated with crustal magnetic fields: positive (negative) potentials for shallow (steep) magnetic elevation angles
- Potential structures also vary with solar zenith angle, solar wind pressure, and EUV irradiance; explanation awaits detailed modeling

Supporting Information:
- Supporting Information S1
- Data Set S1
- Data Set S2
- Data Set S3
- Data Set S4
- Data Set S5
- Data Set S6
- Data Set S7
- Data Set S8
- Data Set S9
- Data Set S10
- Data Set S11
- Data Set S12
- Data Set S13
- Data Set S14
- Data Set S15
- Data Set S16
- Data Set S17
- Data Set S18

Correspondence to:
R. J. Lillis,
rlillis@ssl.berkeley.edu

Citation:
Lillis, R. J., Halekas, J. S., Fillingim, M. O., Poppe, A. R., Collinson, G., Brain, D. A., & Mitchell, D. L. (2018). Field-aligned electrostatic potentials above the Martian exobase from MGS electron reflectometry: Structure and variability. *Journal of Geophysical Research: Planets*, *123*. https://doi.org/10.1002/2017JE005395

Received 18 JUL 2017
Accepted 6 DEC 2017
Accepted article online 18 DEC 2017

1. Introduction

Broadly, Mars's induced magnetosphere is produced by the solar wind's interaction with Mars's upper atmosphere and exosphere via mass loading and with the conducting obstacle of Mars's mostly photo-produced dayside ionosphere. The result is a bow shock, behind which is a turbulent magnetosheath where the solar wind plasma slows, heats up, and is diverted around the obstacle. The interplanetary magnetic field (IMF) embedded in the solar wind piles up in front of the obstacle and drapes around it, forming a double-lobed magnetotail behind Mars (e.g., Brain, 2007; Nagy et al., 2004).

Within this broad picture lies a rich array of electrodynamic and plasma processes, the result of (a) the strong and spatially inhomogeneous crustal magnetic fields rotating with the solid planet and coupling with the

draped IMF; (b) heliospheric structures such as IMF sector boundaries, stream interaction regions, and coronal mass ejections convecting through the system; and (c) solar flares and solar energetic particle events causing episodic but sometimes intense ionization of neutrals. The linkage between the collisional ionosphere and the magnetosheath/tail occurs via matter and energy transport. Particles precipitate into the Mars atmosphere in several forms: solar energetic ions (e.g., Leblanc et al., 2002; Lillis et al., 2016) and electrons (Schneider et al., 2015), neutral hydrogen from solar wind proton charge exchange (Halekas et al., 2015; Kallio & Barabash, 2001), solar wind protons (Diéval et al., 2013), planetary ions (Hara et al., 2013, 2017; Leblanc et al., 2015), and solar wind/magnetosheath electrons (e.g., Lillis & Brain, 2013; Xu et al., 2014).

This paper focuses on the precipitation of these solar wind and sheath electrons. The manner in which this precipitation occurs is influenced by a number of processes occurring in the upper ionosphere and magnetosphere. These include magnetic reconnection (Eastwood et al., 2008; Harada et al., 2015), the guiding of electrons along crustal magnetic field lines toward or away from certain geographic regions (Brain et al., 2007; Lillis & Brain, 2013), the formation and behavior of upward and downward current sheets (Halekas et al., 2006; Halekas & Brain, 2010), and the acceleration of electrons (Brain, Halekas, et al., 2006; Halekas et al., 2007; Lundin et al., 2006). This electron precipitation has a number of consequences, including auroral emission (Bertaux et al., 2005; Leblanc et al., 2008) and ionization (Lillis et al., 2011; Lillis, Fillingim, et al., 2009), the latter of which provides the plasma for ionospheric current systems on the nightside (Fillingim et al., 2010; Riousset et al., 2014). These current systems can close within the ionosphere and/or through the magnetosphere (Dubinin et al., 2008).

Ionosphere–magnetosphere currents can be enhanced by electrostatic potentials/fields parallel to the magnetic field lines. In this study we explain how such parallel potentials can be detected via their effects on suprathermal electron energy and pitch angle distributions measured by the Mars Global Surveyor (MGS) magnetometer/electron reflectometer (MAG/ER) instrument in Mars' orbit. Section 2 describes the instrumentation and electron energy-pitch angle data set used in this study. Section 3 describes the method by which the shapes of electron loss cones are used to constrain both magnetic mirror and electrostatic forces on precipitating electrons and hence provide an estimate of electrostatic potential, with substantially more detail provided in Appendices A and B. Section 4 describes the resulting data set of the derived potentials and their distribution geographically and with respect to relevant variables such as solar zenith angle. Section 5 describes the results, including the average geographic structure of the derived electrostatic potentials, the relationship with crustal magnetic fields, and the variability with respect to external variables such as solar EUV and proxies for solar wind pressure and IMF direction. Section 5.3 discusses the relationship between currents and potentials and possible electrodynamic scenarios to explain our observations.

2. Data Used in This Study

2.1. MGS MAG/ER

The MAG/ER experiment onboard MGS consisted of two triaxial fluxgate magnetometers (Acuña et al., 2001) and a hemispherical imaging electrostatic analyzer that sampled electron fluxes in sixteen 22.5° × 14° angular sectors, spanning a 360° × 14° field of view. Electron fluxes in each sector were measured in 19 logarithmically spaced energy channels from 10 eV to 20 keV. With knowledge of the magnetic field vector measured onboard, the field of view was mapped into pitch angle (i.e., the angle between an electron's velocity vector and the local magnetic field). During one integration (2 s to 8 s), the ER measured between 8% and 100% of the 0°–180° pitch angle spectrum, depending on the orientation of the magnetic field with respect to the field of view plane of the instrument (Mitchell et al., 2001). In this study we use pitch angle distributions (PADs) measured during the MGS mapping orbit phase, from April 1999 to November 2006 (when MGS was lost) at an altitude of 370–430 km and in a sun-synchronous trajectory fixed at 2 A.M./2 P.M. local time.

2.2. Loss Cones in MAG/ER Data

In a uniform magnetic field, electrons move along helical paths of constant radius and pitch angle α. However, if the field strength (B) increases toward the planet (as is the case for regions of Mars with magnetized crust; Lillis et al., 2004), electrons are reflected back along the lines of force if α reaches 90°. If reflection occurs at sufficiently high altitude (before any significant scattering by the collisional atmosphere), then the reflected electrons return to the spacecraft after a round-trip time of ~0.1 s (for ~200 eV) with the same energy and a pitch angle of $180° - \alpha$, according to the adiabatic condition, at least in the absence of significant high-frequency waves below the spacecraft that can modify these pitch angles. Downgoing electrons

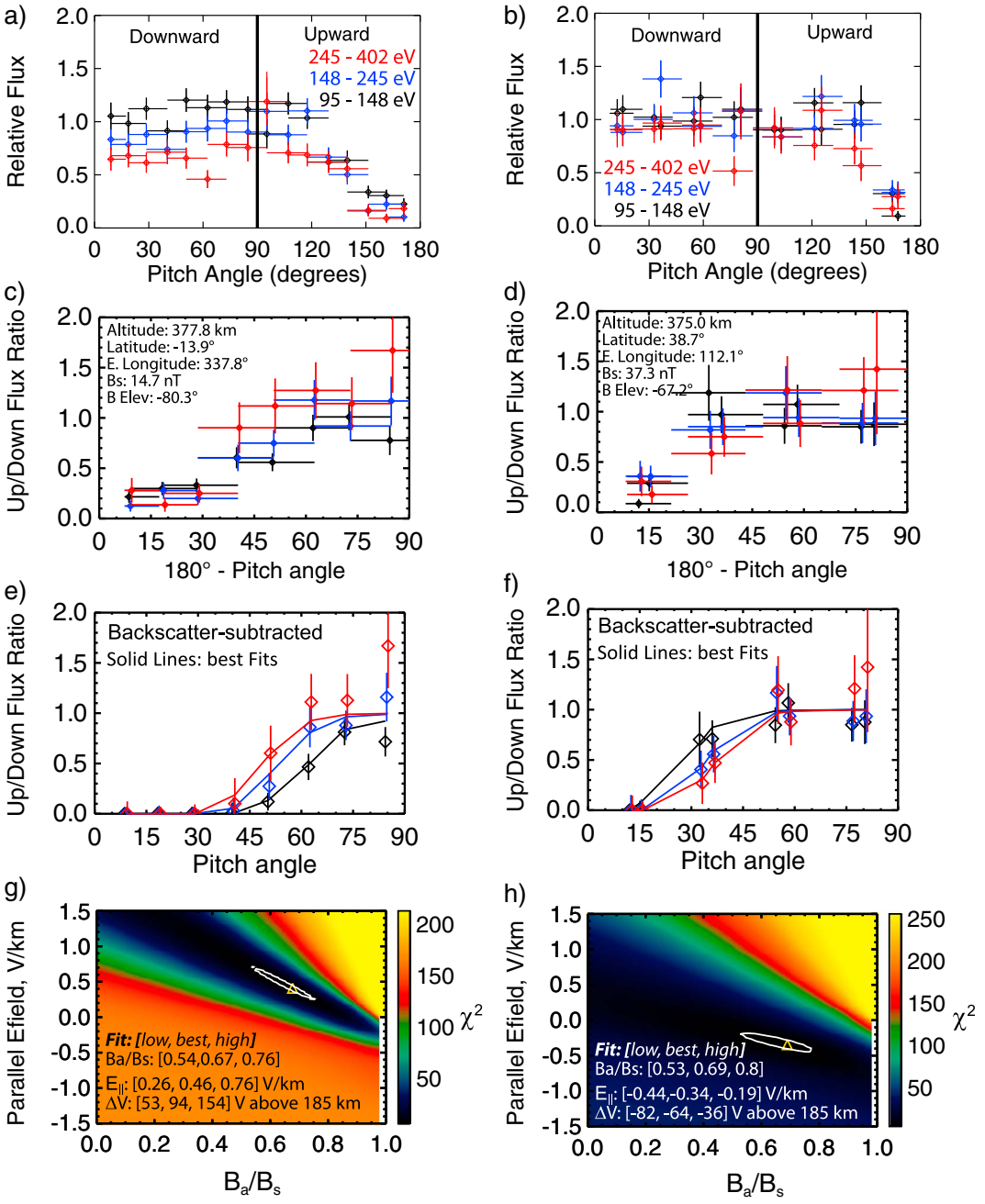

Figure 1. Two examples of constraining field-aligned electrostatic potentials over the altitude range of 185–370 km using suprathermal electron pitch angle distributions (PADs). The left and right columns are examples of radially upward and downward derived field-aligned potentials, respectively. (a, b) The pitch angle distributions in three adjacent energy channels 95–148 eV (black), 148–245 eV (blue), and 245–402 eV (red) with the upward-traveling and downward-traveling sides of the PAD labeled. (c, d) The ratios of upward to downward electron flux at conjugate pitch angles (e.g., flux at pitch angle α divided by the flux at pitch angle $180 - \alpha$ or vice versa depending on the direction of the magnetic field). (e, f) Adiabatic loss cones, that is, ratios of upward to downward flux after backscattered flux has been subtracted using the technique of Lillis, Mitchell, et al. (2008; section 5.3 thereof). Solid lines show the best fits to those flux ratios. (g, h) The χ^2 surfaces and 1-sigma error ellipsoids in the parameter space defined by B_a/B_s and $E_{||}$. The best-fit values of B_a/B_s and $E_{||}$ (which result in the solid lines in Figures 1e and 1f) are shown with orange triangles.

with measured pitch angles further from 90° have lower reflection altitudes and hence a higher probability of being scattered and/or absorbed by the atmosphere, so the flux of upgoing electrons exhibits a larger attenuation for pitch angles further from 90°, known as a *loss cone*. When MGS intersects an "open"

magnetic field line (i.e., one that is connected both to the collisional atmosphere and to the IMF), MAG/ER observes a loss cone PAD, examples of which are shown in Figure 1. The pitch angle past which the reflecting electrons encounter the collisional atmosphere, as well as the shape of the loss cone, are determined by cross sections of dominant electron-neutral collisions and by the profiles, along the magnetic field line to which the electrons are bound, of three quantities: (1) the magnetic field magnitude, (2) the neutral density, and (3) the electrostatic potential, between the spacecraft altitude of 370–430 km and the altitude range of significant electron absorption, as discussed in detail by Lillis, Mitchell, et al. (2008). MAG/ER obtains the most reliable loss cone measurements in three adjacent energy channels: 90–145 eV, 145–248 eV, and 248–400 eV, for which the absorption altitude range is ~150–210 km. This energy restriction exists due to (a) unknown spacecraft potential affecting measurements in the lowest energy channels, (b) a ~40 times smaller instrument geometric factor below 90 eV, and (c) insufficient counts above 400 eV to reliably measure loss cone shapes in enough PADs. More than 10 million loss cone PADs were measured by MAG/ER, which we will use for analysis in this paper.

3. Method: Measuring Field-Aligned Electrostatic Potentials

In the simplest form of this problem, with a magnetized hard absorber such as a planetary surface, nearly all electrons that do not magnetically reflect above the surface are absorbed by that surface. In this case, electron loss cones are very close to step functions, and field-aligned potential differences can be quite straightforwardly derived from the energy dependence of the loss cone angle, as has been demonstrated at the Moon (Halekas et al., 2008; Halekas et al., 2005). Below we describe how such potentials are derived in the complicating case of an absorbing atmosphere.

3.1. Modeling Loss Cone Formation

The mathematical details of the dependence of loss cone shapes on these quantities, as well as the kinetic electron transport modeling and data analysis techniques required to constrain them, using MAG/ER PADs, are explained by Lillis, Mitchell, et al. (2008) and are summarized below. We express the probability of a downward-traveling electron of initial kinetic energy U_0 and initial pitch angle α_0, scattering off an atmospheric neutral particle as a function of the distance x that it moves along the field line:

$$P_{\mathrm{scatt}}(\alpha_0, U_0, x) = 1 - \exp\left[-\sum_i \sum_j \int_0^x \frac{\sigma_{ij}\left(U\left(x'\right)\right) n_i\left(x'\right) \mathrm{d}x'}{\sqrt{1 - \sin^2\alpha\left(x'\right)}}\right] \tag{1}$$

where the summations are over all neutral species i and all collision processes j, where $n_i(x)$ is the neutral density of species i, $U(x)$ is the electron's energy as a function of distance along the field line, $\sigma_{ij}(U(x))$ is the energy-dependent cross section for electron scattering off a neutral particle i via process j, and $\alpha(x)$ is the electron's pitch angle. The numerator inside the integral accounts for scattering (i.e., it increases linearly with both cross section and the density of scatterers), while the denominator accounts for the effective increase in path length due to the electron's gyro motion around the field line.

As it moves along the field line, the electron's kinetic energy $U(x)$ will increase or decrease as it is accelerated or decelerated by the parallel electrostatic potential $\Delta V(x)$.

$$U(x) = U_0 - e\Delta V(x) \tag{2}$$

where e is the electronic charge. The electron's pitch angle evolution $\alpha(x)$ is determined by the adiabatic condition and hence by the variation in both the magnetic field $B(x)$ and the potential $\Delta V(x)$.

$$\sin^2\alpha(x) = \frac{B(x)}{B_0} \frac{\sin^2\alpha_0}{\left(1 - \frac{e\Delta V(x)}{U_0}\right)} \tag{3}$$

We express the magnetic field magnitude along the field line as the sum of a constant, ambient component and a crustal component that increases as distance to crustal magnetization decreases:

$$B(x(z)) = B_a + (B_s - B_a)\left(\frac{z_s}{z}\right)^p \tag{4}$$

where z is the distance from the crust along the field line, B_a is the ambient (i.e., non-crustal) component of the field, B_s is the field measured at the MGS spacecraft, and p is a power law exponent for the altitude dependence of the crustal magnetic field. The magnetic field profile is therefore determined by p and the ratio B_a/B_s

(convenient because it is dimensionless and ranges between 0 and 1). $p = 2.0$ would be appropriate for an infinite line of crustal dipoles and 3.0 for a single dipole. Lillis, Frey, Manga, Mitchell, et al. (2008) showed that loss cone shapes measured by MAG/ER are not separately sensitive to both p and B_a/B_s within this reasonable range of $p = 2$ to 3 and that we can therefore fix $p = 2.5$ and vary B_a/B_s to reflect different strengths of crustal magnetic field.

Insufficient information is contained within the loss cones shapes to constrain the specific profile of the electrostatic potential difference between the spacecraft and absorption region (Lillis, Mitchell, et al., 2008). Therefore, in the absence of a priori information, we parameterize it by a constant electric field $E_{||}$ parallel to the magnetic field.

$$\Delta V(x) = E_{\|} x \tag{5}$$

We define positive parallel electrostatic potentials/electric fields to point vertically upward and negative potentials downward. Thus, positive potentials accelerate the negatively charged electrons downward toward the absorbing atmosphere, reducing the fluxes that can travel back up the field line to the spacecraft, thereby causing loss cones to shift nearer to 90° pitch angle. In contrast, negative potentials push the electrons up and away from the atmosphere, increasing the fluxes that can travel back up the field line, thereby causing loss cones to shift further from 90° pitch angle. This shift in loss cone angle is greater for lower energies because the electrostatic potential is a larger fraction of their total energy. This energy-dependent loss cone shift is illustrated in section 5.2 of Lillis, Mitchell, et al. (2008) and is in contrast to changes in the neutral density or magnetic field profiles, which cause loss cone shifts that are almost energy-independent.

We can use equations (1)–(5) to model the formation of loss cones as a function of energy under any combination of neutral atmosphere profile, crustal field strength (parameterized by the ratio B_a/B_s), and electric field $E_{||}$. We do this in two complementary ways. The first method is comprehensive, whereby we send hundreds of thousands of electrons down into the atmosphere at 3° increments of initial pitch angles, simulating every collision to correctly account for atmospheric scattering. This model is called MarMCET (Mars Monte Carlo electron transport) and is explained and applied in several publications (e.g., Lillis & Fang, 2015; Lillis, Frey, & Manga, 2008; Lillis, Mitchell, et al., 2008; Lillis et al., 2011). The second method ignores multiple scattering of electrons, calculating only the probability that a downward-traveling electron at pitch angle α will be reflected (magnetically and/or electrostatically) back to the spacecraft altitude at $180 - \alpha$ without scattering. Loss cones calculated this way are called "adiabatic" because the electrons that survive conserve the first adiabatic invariant of charged particle motion (e.g., Parks, 2004). This method is computationally more than 1 million times faster than the first, allowing rapid calculation of loss cones for a large range of values of B_a/B_s and $E_{||}$.

3.2. Fitting Procedure to Constrain Field Aligned Potentials

It would be prohibitively time-consuming to use the MarMCET model to iteratively fit (i.e., typically dozens of loss cone simulations) each of ~10 million measured loss cones for the best-fit values of B_a/B_s and $E_{||}$. Instead, we take advantage of a useful property of loss cone formation. Consider the ratio of flux of upward-traveling electrons measured at a given pitch angle that have been scattered at least once by atmospheric neutrals to the total flux of upward-traveling particles (i.e., the sum of these "backscattered" electrons plus electrons that have been reflected back upward solely by magnetic gradient or electrostatic forces) at the same pitch angle. Lillis, Mitchell, et al. (2008) showed that this ratio is a known function only of the dimensionless total scattering depth (akin to an optical depth, but for electrons) of atmosphere through which a nonscattering electron would pass. They also showed that this allows us to quickly and efficiently subtract the backscattered component of the measured PAD, leaving a good approximation of the loss cone shape as it would be measured if all electrons that scatter off atmospheric neutrals were absorbed by the atmosphere, that is, an adiabatic loss cone.

For each measured PAD, we simultaneously fit our fast adiabatic model of loss cone formation to the backscatter-subtracted loss cone shapes in all three electron energy channels (90–145, 145–248, and 248–402 eV). We employ an adaptive-step gradient search algorithm called "amoeba" (because it "slithers" around a parameter space (Press et al., 1992) like that shown in Figures 1g and 1h) to find the minimum misfit (reflected by the classic χ^2 metric; e.g., Bevington & Robinson, 2003) and hence the best-fit values of B_a/B_s and $E_{||}$ for that PAD. For the neutral density profile in the model, we use the same mean reference model atmosphere described in Appendix A of Lillis, Frey, Manga, Mitchell, et al. (2008) for all cases. As was mentioned

earlier and explained by Lillis, Bougher, et al. (2008), increasing (decreasing) atmospheric density profiles shifts loss cones closer to (further from) 90° in an almost-energy-independent way. Typical examples of our fitting procedure are shown in Figure 1, including the χ^2 surface and 1-sigma error ellipsoid, for both positive and negative derived values of field-aligned electrostatic potentials. Note that the best-fit values of B_a/B_s from the entire MGS MAG/ER data set were used to construct the map of crustal magnetic field magnitude at 185 km altitude (which is the average altitude of greatest sensitivity of loss cone shape to magnetic field strength) published in Lillis, Frey, Manga, Mitchell, et al. (2008) and used in several geophysical studies subsequently (e.g., Lillis, Dufek, et al., 2009; Lillis, Frey, & Manga, 2008; Lillis, Robbins, et al., 2013; Lillis, Stewart, et al., 2013; Lillis et al., 2010, 2015; Robbins et al., 2013).

Note that the example PAD in Figure 1a (where the derived field-aligned potential is positive) appears to be a typical loss cone in all three energy channels, that is, downward-traveling electrons from the Martian magnetotail are precipitating into the atmosphere and then scattering and magnetically reflecting back upward in a pitch angle dependent way, as discussed in section 2.2.

Figure 1 also illustrates that the uncertainties in any one determination of field-aligned potential can be quite large. Therefore, we will not analyze individual orbits in this paper. Instead, we will concentrate on broad trends in these potentials with respect to variables we expect to play a role in maintaining potentials: geographic location, crustal magnetic field strength, magnetic elevation angle, solar wind pressure proxy, solar zenith angle, and so on.

3.3. Validation and Correction of Derived Values of $E_{||}$

The examples shown in Figure 1 are typical of this large data set. However, because the typical loss cone shifts are small with respect to the pitch angle bin widths and the uncertainties are large, we wish to provide a statistically significant demonstration that our fitting procedure (including the backscatter subtraction step) is indeed capable of estimating field-aligned potentials. The interested reader is directed to Appendix A where we show a clear, intuitively understandable energy-dependent pattern in the measured loss cone shapes for similar derived values of B_a/B_s and $E_{||}$.

As well as the uncertainties in the derived values of $E_{||}$ discussed in Section 3.2, our ability to constrain the field-aligned potential is also limited by the physics of loss cone formation. If the magnetic field-aligned potential below the spacecraft is too strongly positive (upward), then the negatively charged electrons are pulled downward into the collisional atmosphere and none will magnetically reflect back upward to provide a measure of the loss cone angle and no value of $E_{||}$ is thus derived. The weaker the magnetic mirror force (i.e., the larger the value of B_a/B_s), the smaller the upward potential that is required for this situation to occur. The result is that mean values of $E_{||}$ are biased negative for the highest values of B_a/B_s. Appendix B explains this bias in more detail and describes how we correct for it. The correction is largest in regions of extremely weak crustal magnetic field, such as the Tharsis volcanic province (Lillis, Dufek, et al., 2009) and Utopia Planitia (Lillis, Frey, Manga, Mitchell, et al., 2008), and is typically on the order of +0.01 V/km. This may not seem like a large amount but it corresponds to $>$~2.1 V over the distance between the MGS spacecraft and the collisional atmosphere and is sufficient to shift the derived values of $E_{||}$ from slightly negative to approximately zero in large regions on the nightside, as discussed in the next section.

4. Data Set of Electrostatic potentials

The fitting algorithm results in a reliable fit for approximately 40% of measured loss cones. Poor fits in the remainder result from a combination of (a) insufficient fluxes to accurately determine loss cone shapes in more than one energy channel, (b) insufficient pitch angle coverage to measure a loss cone (recall that the instrument only has a 14° × 360° field of view, so pitch angle coverage depends on the magnetic field direction, varying between 14° and the full 180°), and (c) non-gyrotropy, that is, substantially different fluxes measured on opposite sides of the instrument anode (i.e., at the same pitch angle but different gyro phase). This leaves ~3.6 million derived average values for the parallel component of electric field between ~180 km and 370–430 km at 2 A.M./2 P.M. solar local time. We convert these to a potential difference in volts between the spacecraft and 185 km altitude by making the necessary assumption that the magnetic field lines are straight over this distance, with the same elevation angle as measured at the spacecraft. This leads to a small

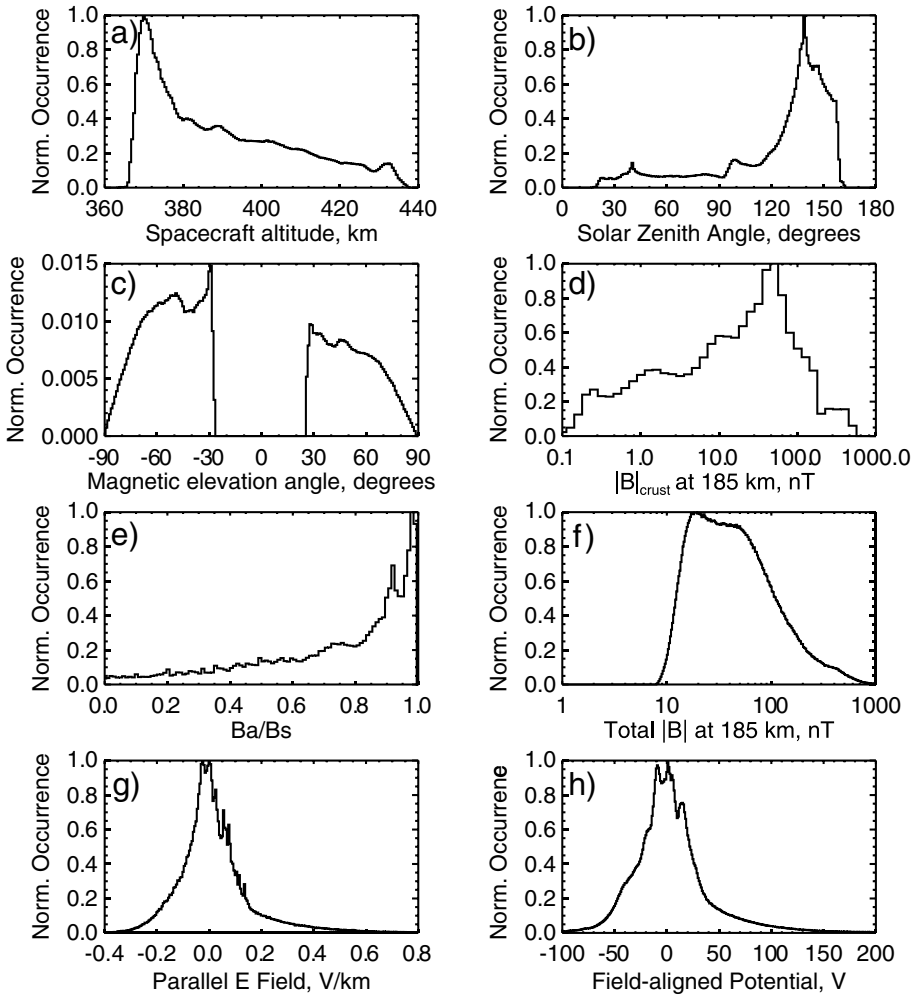

Figure 2. Histograms of some key variables analyzed in this study, as follows: (a) altitude of the spacecraft, (b) solar zenith angle of MGS, (c) magnetic elevation angle, and (d) crustal magnetic field magnitude at 185 km altitude from the map of Lillis, Frey, Manga, Mitchell, et al. (2008). (e, f) B_a/B_s and the total (i.e., crustal plus external) value of magnetic field at 185 km that is derived therefrom (Lillis et al., 2004), respectively. (g, h) $E_{||}$ in V/km and the associated field-aligned potential ΔV between the spacecraft and 185 km altitude, respectively.

underestimation in the potential where field lines are strongly curved but is a reasonable assumption for the great majority of cases, as shown in Appendix D of Lillis, Frey, Manga, Mitchell, et al. (2008).

We begin with a high-level survey of the data set. Figure 2 shows histograms of the important variables defining the data set. It shows variables that are important for determining field-aligned potential: spacecraft altitude, magnetic elevation angle, solar zenith angle, and strength of the crustal magnetic field at 185 km. Magnetic elevation angle has a sharp cutoff around 30° because we discard cases where the straight-line extension of magnetic field lines from the spacecraft altitude does not connect to our nominal electron exobase (185 km on average; Lillis, Mitchell, et al., 2008). The solar zenith angle histogram reflects the fact that loss cones do not form as easily in the draped magnetic topology of the dayside (Brain et al., 2007). It also shows histograms of the two variables derived directly from fitting our model to each PAD: B_a/B_s and $E_{||}$, as well as physical parameters derived from those quantities, that is, the coderived total magnetic field magnitude at 185 km and the associated field-aligned potential ΔV. Seasonal coverage is approximately uniform (not shown).

Figure 3 shows two-dimensional histograms in planetary latitude and longitude of the data set, divided up into measurements on the dayside (which we define to be solar zenith angle (SZA) $< 70°$), in the terminator region ($70° <$ SZA $< 110°$), and on the nightside (SZA $> 110°$). We choose 110° as the (somewhat arbitrary) boundary between the terminator and nightside because the entire altitude range over which we are sensitive to field-aligned potentials (~200–400 km) is in sunlight for SZA $< 110°$.

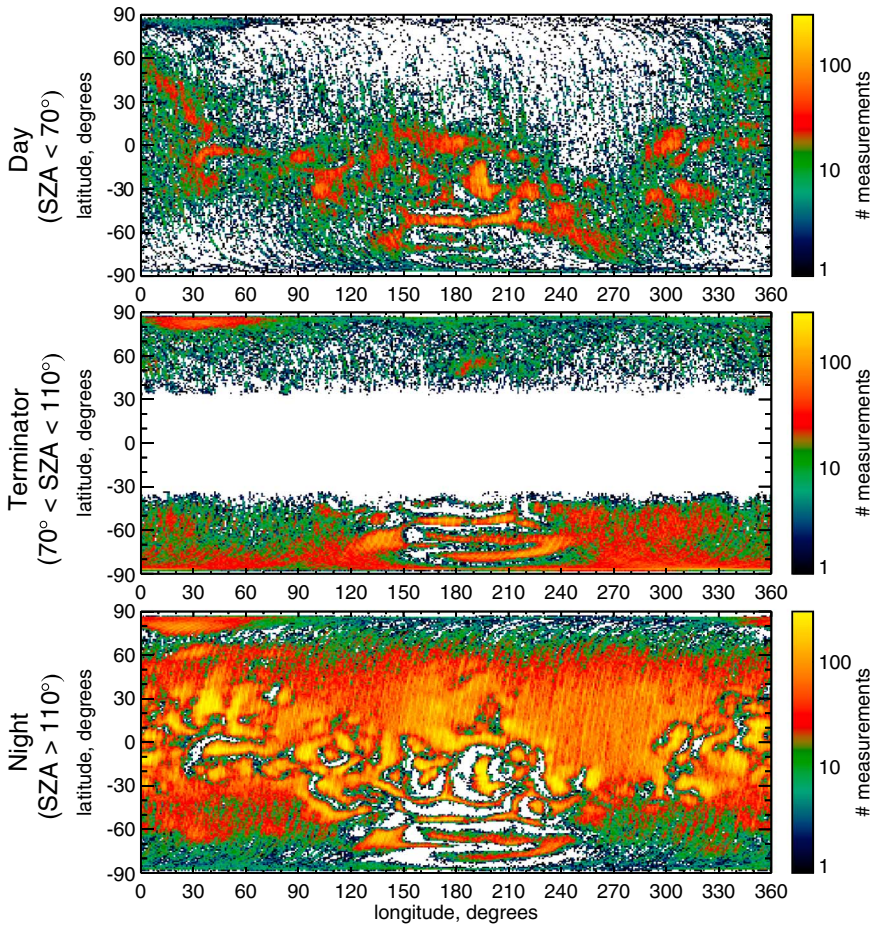

Figure 3. The number of valid retrievals of $E_{||}$ (and hence ΔV) in each 1° × 1° bin of latitude/longitude, demonstrating the geographic distribution of data on the dayside (SZA < 70°), terminator region (70° < SZA < 110°), and nightside (SZA > 110°), respectively.

As mentioned above, the solar zenith angle distribution and geographic distribution matches the locations where loss cones preferentially form, as shown by Brain et al. (2007) and Lillis, Frey, Manga, Mitchell, et al. (2008), that is, where magnetic field lines connect the collisional atmosphere with the draped interplanetary magnetic field. Away from strong crustal magnetic fields (concentrated mostly in the southern hemisphere between 120° and 240° E), this favorable magnetic topology occurs more frequently on the nightside where the magnetotail is predominantly sunward–anti-sunward than on the dayside where the draped field is predominantly tangential to the planet. We also see measurements, on both the day and night side, where crustal magnetic fields are strong and vertical. We notice very few measurements where magnetic fields are predominantly horizontal, for example, strong crustal fields in the southern hemisphere (appearing like channels of no data between long islands of measurements where the crustal field is vertical) and on the dayside away from strong crustal fields. For reference, Figure 4 shows the same geographic map area with contours of the radial component of the crustal magnetic fields.

5. Results

In examining this data set, we shall divide our analysis into two main areas: average structures and variability. The former is concerned with the average pattern, built up over tens of thousands of orbits, of field-aligned potentials with respect to Mars's crustal magnetic fields, in the three solar zenith angle bins shown in Figure 3. The latter is concerned with variability, both statistical (i.e., the natural variability of the system) and with respect to external conditions such as solar wind pressure, IMF direction, and season.

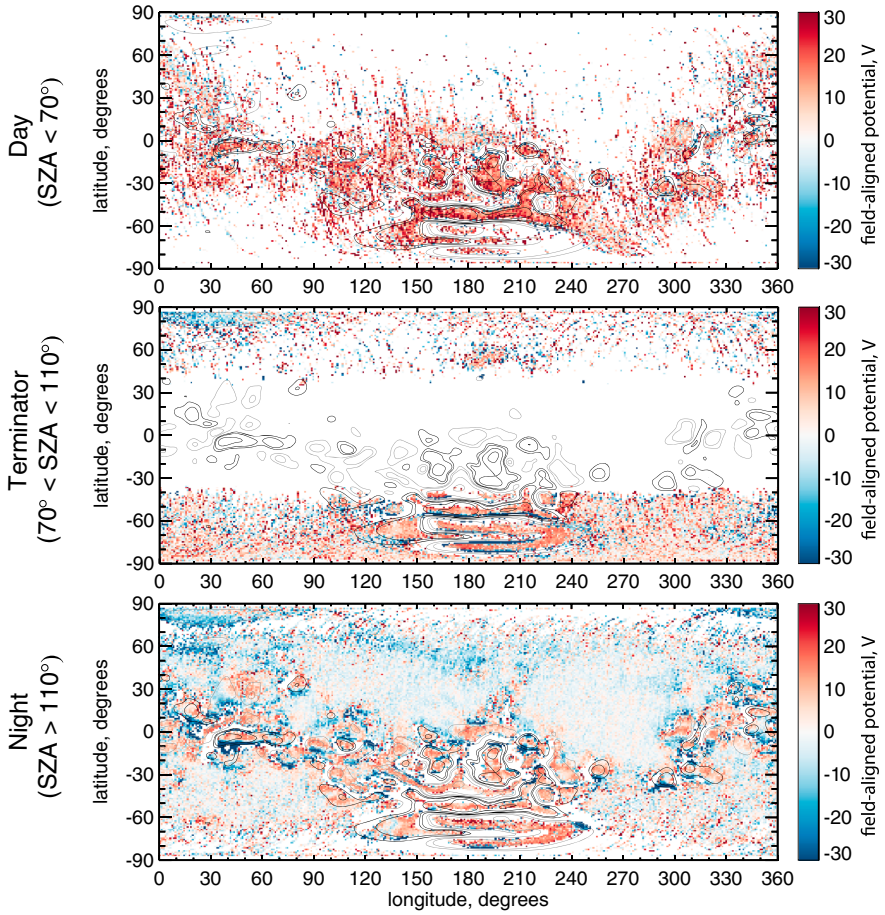

Figure 4. Maps of field-aligned potential between 185 km and MGS (370–430 km) for three ranges of solar zenith angles (SZAs): (top) SZA < 70° (day), (middle) 70°<SZA < 110° (terminator), and (bottom) SZA > 110° (night). Median values of field-aligned potential derived from the complete data set (May 1999 until November 2006) are shown in 1° × 1° bins. Contours of positive (black) and negative (grey) radial crustal magnetic field at 400 km from the spherical harmonic model of Morschhauser et al. (2014) are overlaid (±10, 20, and 50 nT).

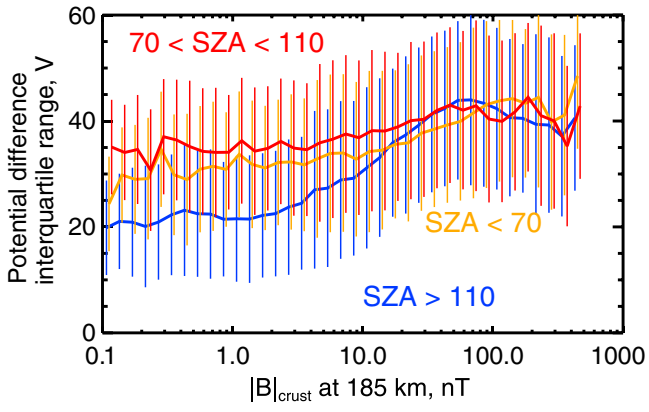

Figure 5. Variation of ΔV within each 1° × 1° geographic pixel. Means and standard deviations of interquartile ranges (i.e., 75th minus 25th percentile) of ΔV for the same pixels shown in Figure 4 are plotted for each of 40 crustal field strength bins. Blue represents the nightside (SZA > 110°), red represents the terminator region (70° < SZA < 110°), and orange represents the dayside (SZA < 70°).

5.1. Average Structure of Field-Aligned Potentials

First, we wish to examine the global geographic distribution of field-aligned electrostatic potentials. We find it instructive to divide the data set into measurements taken on the dayside, terminator, and nightside, as discussed in the previous section. Figure 4 shows the median field-aligned potential ΔV in 1° × 1° longitude/latitude bins over the entire data set, separately for dayside, terminator, and nightside (similarly to Figure 3), while Figure 5 shows the accompanying interquartile range as a function of crustal magnetic field strength to give a feeling for the spread of values of ΔV within each pixel. The radial component of crustal magnetic field at 400 km altitude from the spherical harmonic model of Morschhauser et al. (2014) is overlaid on both figures as contours. A few broad observations can be made based on this global map. First, we notice that positive (upward) potentials are generally stronger on the dayside, compared with the terminator or nightside. Second, a broad correlation exists between ΔV and crustal magnetic field strength, for all SZA intervals: the strongest positive and negative values of ΔV occur in regions where the crustal field is also the strongest. Third, where crustal fields are extremely weak (e.g., the large impact basins Hellas and Utopia and the Tharsis volcanic

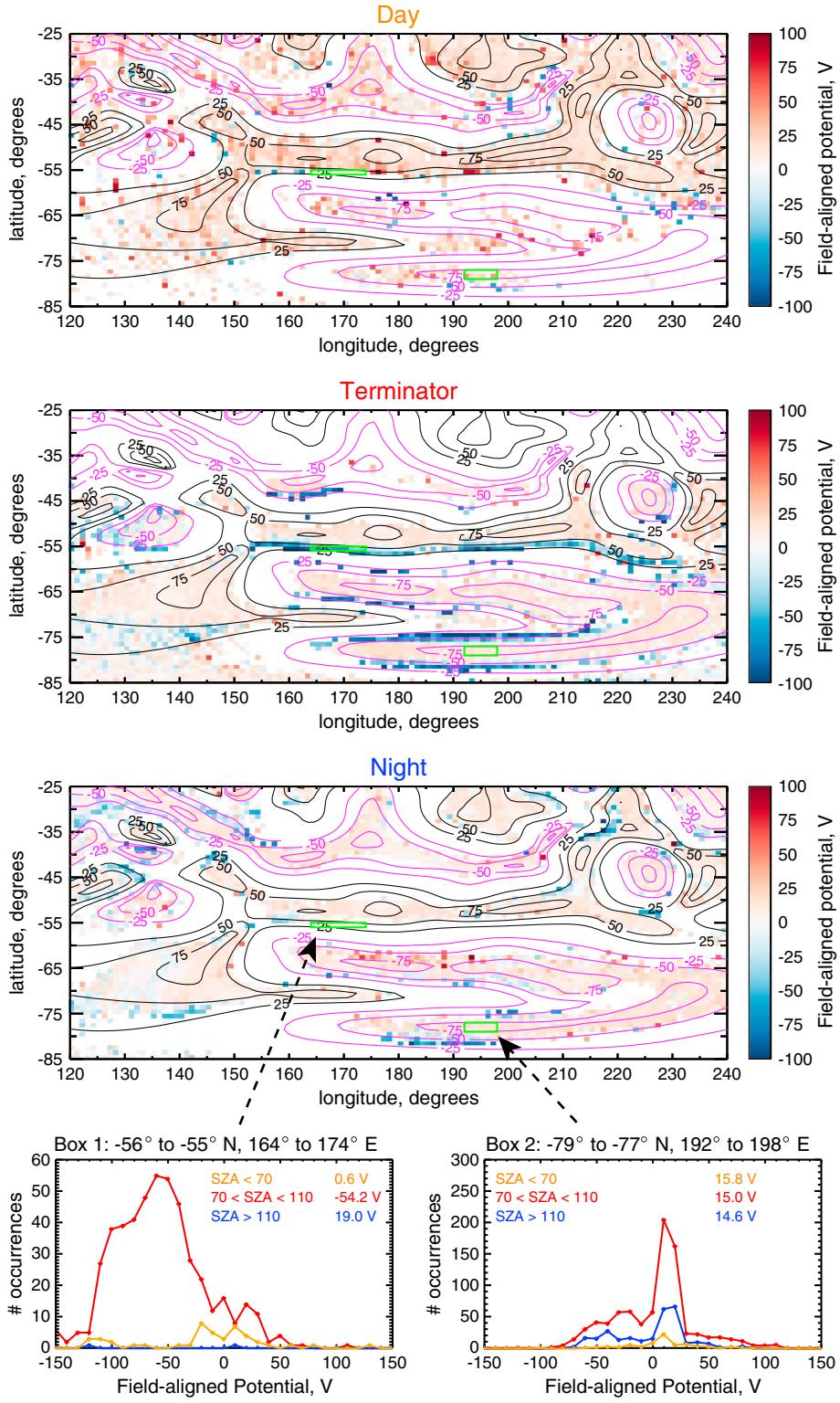

Figure 6. The top three panels show the same data as Figure 4, zoomed into the region of Terra Sirenum and Terra Cimmeria where Mars's strongest crustal fields exist Sinus Sabaeus region. However, the contours are not radial magnetic field, but magnetic elevation angle (i.e., angle from the horizontal) at 400 km in degrees with positive (black) and negative (gray) contours at ±25°, 50°, and 75°. Also, the color scale is wider to accommodate the large negative potentials that exist at the edges of some magnetic cusps. The lower two panels show histograms of field-aligned potential. Different ranges of SZA and median values of DV are represented by different colors.

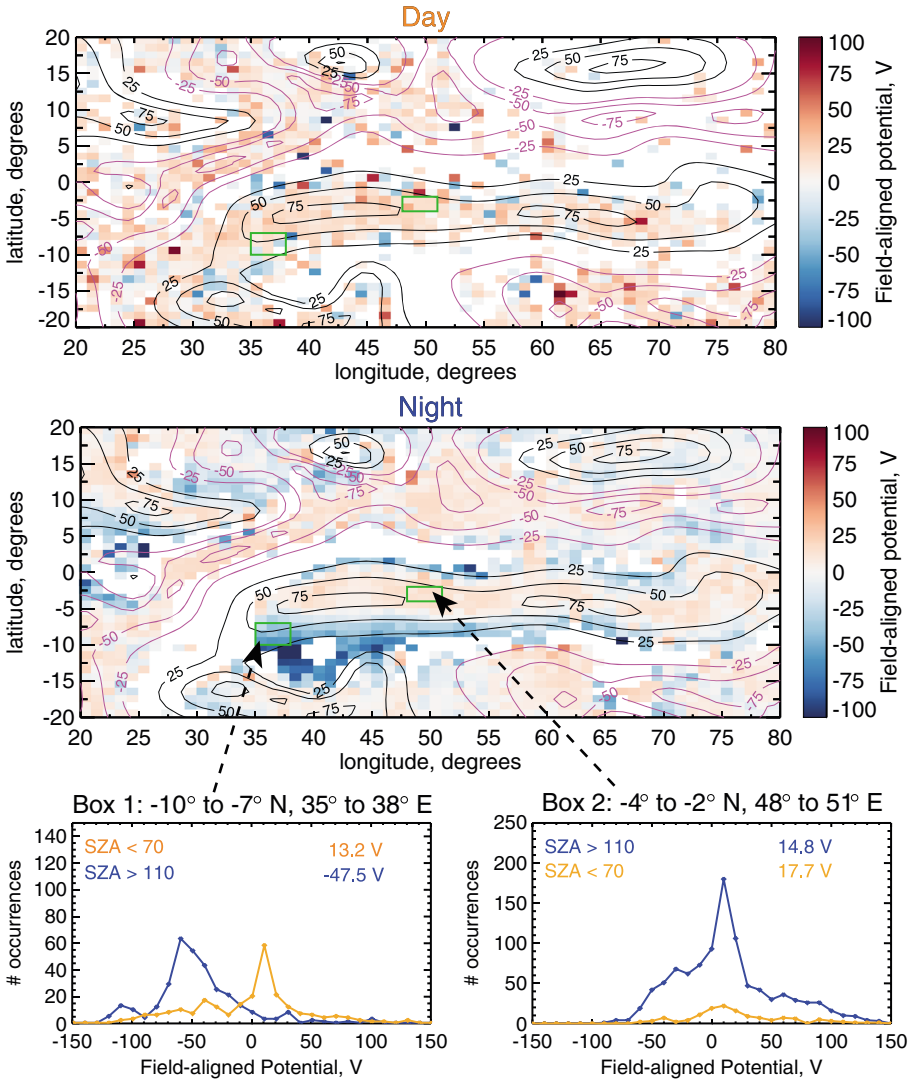

Figure 7. Identical to Figure 6 except for the Sinus Sabaeus region of Mars where also exist moderately strong crustal magnetic fields. Panels are shown only for day (SZA $<$ 70°) and night (SZA $>$ 110°) because MGS's sun-locked polar orbit never samples the equatorial region at the terminator.

region), potentials are indistinguishable from zero on the nightside and slightly positive on the dayside and near the terminator. Fourth, for the nightside and terminator, distinct positive and negative (i.e., blue and red) potential structures are visible where the crustal magnetic fields are strong. The weaker the crustal field, the less distinct and weaker these potential structures appear to be. Fifth and finally, Figure 5 shows that the interquartile range of values within each geographic pixel increases with crustal magnetic field strength, with a slight dependence for the dayside and terminator, and a more pronounced dependence for the nightside. Since the uncertainty in the technique should not depend on crustal field or time of day, Figure 5 shows that there is substantially less natural variability in field-aligned potentials in weak magnetic field regions on the nightside, compared with those same regions on the dayside/terminator or where crustal fields are stronger. Note that no significant dependence of interquartile range on magnetic field elevation angle was found.

In order to examine these distinct positive and negative potential structures in more detail, we zoom in the two strongest crustal magnetic field regions: Figure 6 shows the Terra Sirenum/Cimmeria region, and Figure 7 shows the Sinus Sabaeus region. Note that these figures are similar to Figure 4 except that (a) the range of potentials (color scale) shown are larger and (b) the contours are not radial magnetic field but magnetic elevation angle, so as to more clearly delineate magnetic geometry. Both of these figures also show histograms

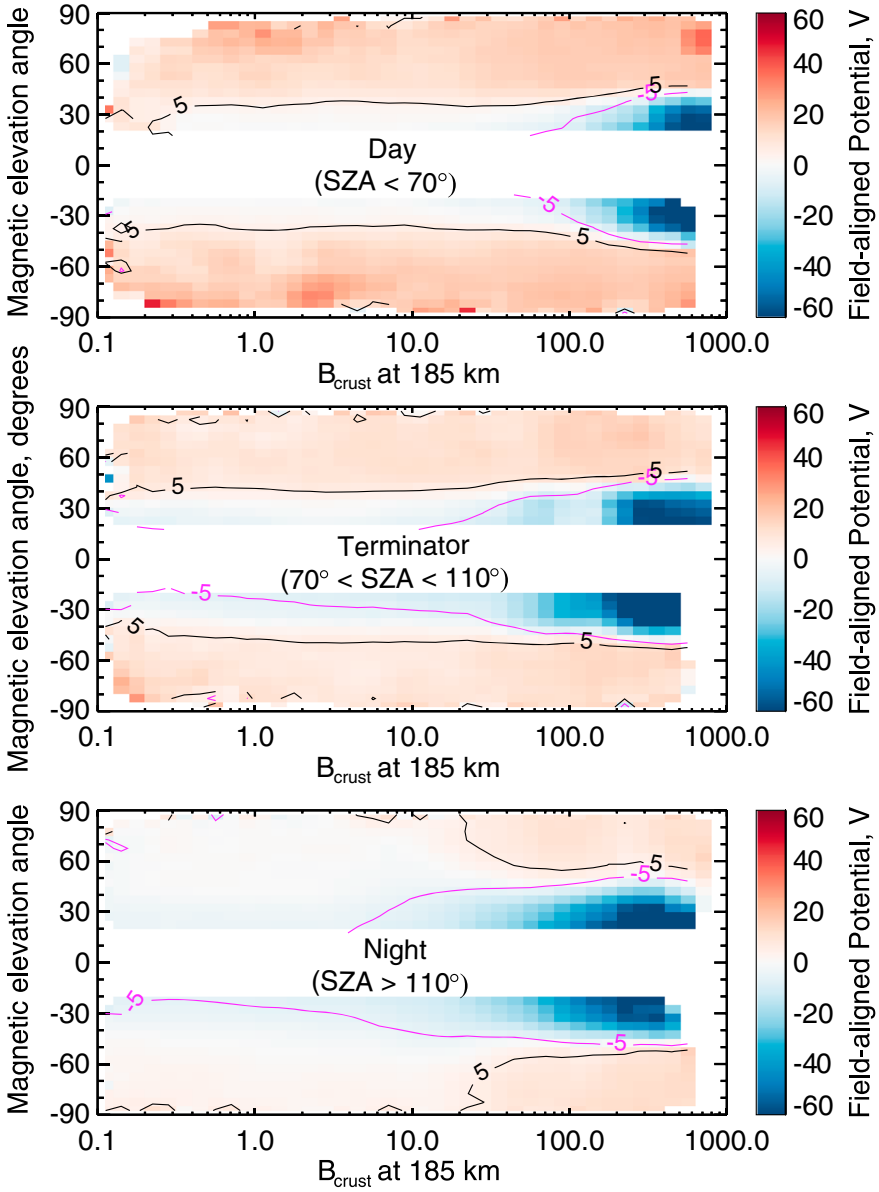

Figure 8. Average field-aligned potential plotted as a function of magnetic elevation angle and crustal magnetic field strength, for three SZA ranges: (top) dayside (SZA < 70°), (middle) terminator region (70° < SZA < 110°), and (bottom) nightside (SZA > 110°). Black and gray contours display the positive and negative 5 V contours, respectively. The color scale is different from either Figure 4 or Figures 6 or 7.

of ΔV for example regions of nearly vertical (~75° elevation angle) and more horizontal (25°–50°) magnetic field. A few characteristics are immediately clear. First, we are limited by where loss cones form based on the connectivity between crustal fields and the draped IMF: Box 1 in Figure 6 has a statistically insignificant three samples on the nightside, but almost 500 in the terminator region. Second, average potentials are positive where magnetic elevation angles are >~50° at the dayside, terminator, and nightside. Note that Box 2 in both figures, near the center of an open crustal magnetic field region (also called a "cusp" by analogy to Earth; Brain et al., 2007) is remarkably consistent at +~15–18 V, regardless of solar zenith angle. Third, where loss cones do form at magnetic elevation angles <~50°, potentials are predominantly (and in some places strongly) negative at night and at the terminator, but generally more positive on the dayside.

Finally, it is useful to examine the relationship between field-aligned potential, magnetic elevation angle, and crustal magnetic field strength in statistical, nongeographic form, as shown in Figure 8, where we see more

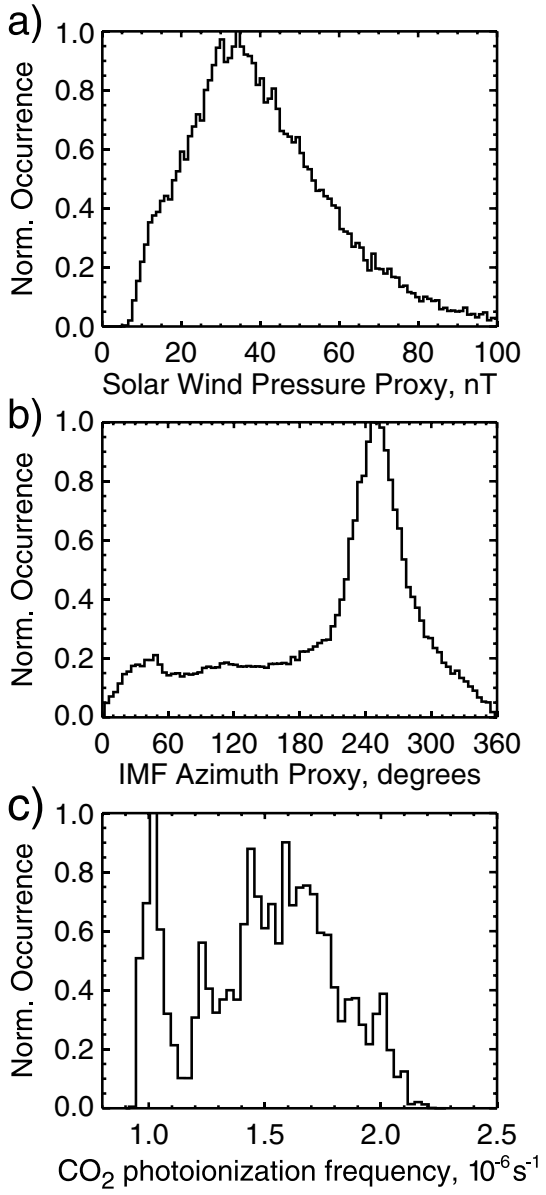

Figure 9. Histograms of external drivers or their proxies measured during the time of the MGS data set that may affect the formation of field-aligned letter set of potentials. (a) Solar wind pressure proxy (Crider, 2003), (b) IMF clock angle proxy (Brain, Mitchell, et al., 2006), and (c) CO_2 photoionization frequency at Mars scaled and shifted from Earth-based assets (Thiemann et al., 2017).

clearly many of the features discernible in Figure 4. The first feature we notice is the strong dependence of field-aligned potentials on magnetic elevation angle. For elevation angles >45°, potentials are generally more strongly positive (red) as one goes from the nightside to the terminator to the dayside; indeed, weak crustal field regions on the nightside show no significant potentials (<5 V) at all. In contrast, for elevation angles <45°, we see typically weak or negative potentials, with stronger negative potentials (blue) forming for stronger crustal fields. As we go from night to terminator to dayside, these negative potentials form at progressively higher crustal field strengths, while negative potentials are similar across all solar zenith angles for the very strongest crustal fields (>400 nT at 185 km). Lastly, the field-aligned potential patterns are almost symmetric between positive and negative magnetic elevation angles (with a mild asymmetry for the terminator case being likely due to the sampling of the relatively smaller number of positive versus negative "cusps"), which makes sense as similar processes should occur regardless of the direction of the magnetic field (Earth's northern and southern aurora exhibit the same features).

5.2. Variability With External Conditions

We now examine how our derived field-aligned electrostatic potentials and their dependence on magnetic elevation angle and crustal field strength vary with three external drivers: solar wind pressure proxy, interplanetary field (IMF) direction proxy, and solar extreme ultraviolet flux (explained below). Figure 9 shows histograms of these three quantities across the data set.

5.2.1. Variability With Solar Wind Pressure Proxy

Given that field-aligned electrostatic potentials are expected to be driven, at least in part, by magnetosheath flow velocity and direction (Dubinin et al., 2008; Lyons, 1980), it makes sense to compare our derived values with solar wind pressure. No direct measurements of the upstream solar wind were made, coinciding with our data set; Mars Express's ion mass analyzer (2004–present) was usually turned off more than 20 min away from periapsis (M. Holmstrom, private communication) and so did not measure solar wind. However, orbit-average dayside MGS magnetometer measurements of field magnitude between 50° and 60° North (i.e., away from crustal magnetic fields) have been shown to be an adequate proxy for solar wind pressure under the assumption that the dynamic pressure of the solar wind is converted to magnetic pressure in the Mars magnetic pileup region (Brain, 2005; Crider, 2003). This proxy has been used as a way to understand the variability of Martian plasma processes in numerous studies since (e.g., Edberg et al., 2008; Lillis & Brain, 2013).

Figure 10 shows how ΔV and its dependence on crustal magnetic field strength vary with solar wind pressure and magnetic elevation angle. For high (i.e., steep) elevation angles, we see the same small positive dependence of upward potentials on crustal field strength as in Figure 8, but no discernible dependence on solar wind pressure. However, for low (i.e., shallow) elevation angles and strong crustal fields, we clearly see smaller negative potentials for higher solar wind pressures on both the day and night sides.

There are a few possible reasons for this. First, higher pressures provide more charge carriers in the magnetosheath, increasing plasma conductivities and therefore decreasing potential differences. Second, on the nightside at least, higher solar wind pressures result in more electron impact ionization in open field regions and therefore more mobile charge carriers in the ionosphere, and hence lower potentials. Third, higher pressures are known to compress Mars's crustal fields (Lillis & Brain, 2013), increasing field

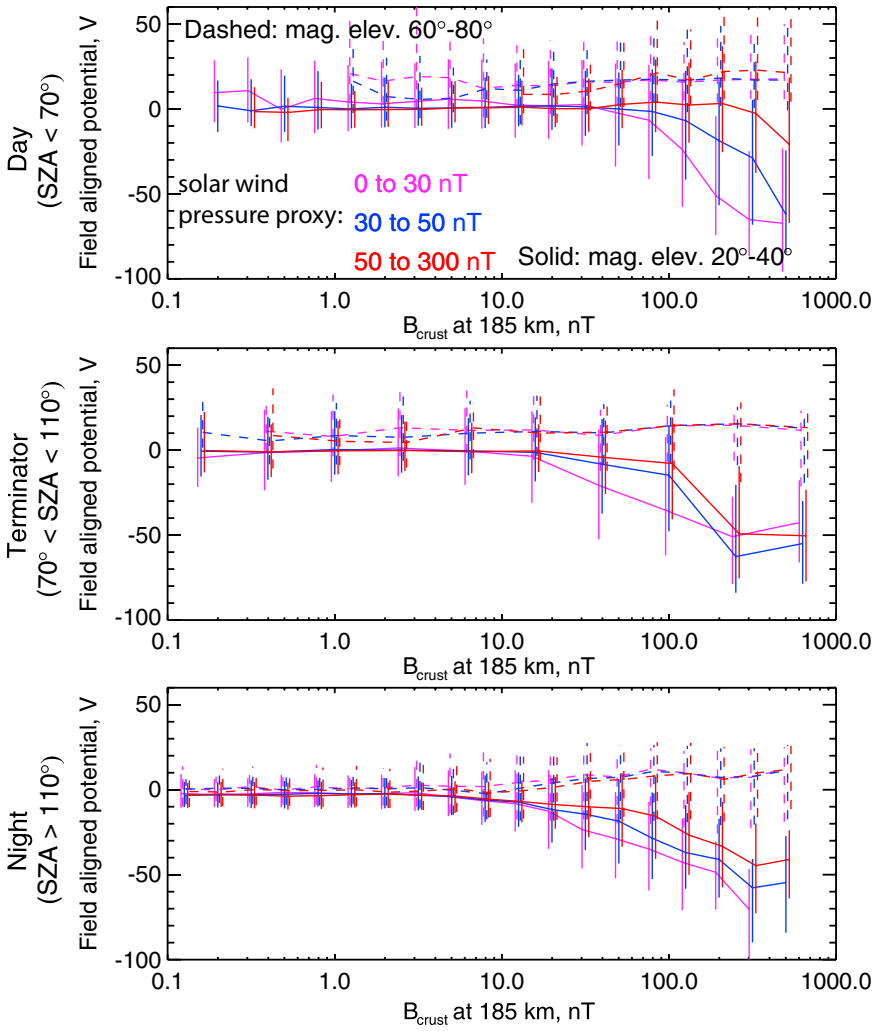

Figure 10. Field-aligned electrostatic potential is plotted as a function of crustal magnetic field magnitude at 185 km (Lillis, Frey, Manga, Mitchell, et al., 2008), for two different ranges of magnetic elevation angle: 20°–40° (solid) and 60°–80° (dashed); and three different ranges of solar wind pressure proxy: 0 to 30 nT (pink), 30 to 50 nT (blue), and >50 nT (red). (top) Dayside (SZA < 70°), (middle) terminator (70° < SZA < 110°), and (bottom) nightside (SZA > 110°) data are shown. Error bars represent the interquartile range, that is, the difference between the 25th and 75th percentiles of all ΔV values in each bin.

curvature and changing field geometry, thereby modifying any plasma kinetic effects that may be responsible for the potentials.

At the terminator, we see a similar pattern up to crustal field strengths of 100 nT but, perhaps due to poor statistics, no discernible dependence on solar wind pressure for stronger crustal fields.

5.2.2. Variability With IMF Clock Angle Proxy

The pattern with which the IMF drapes around Mars and connects (or not) with the crustal fields depends on its direction; hence, we might expect this direction to affect field-aligned potentials. Similarly to the solar wind pressure proxy discussed in the previous section, the direction of dayside magnetic fields measured away from crustal fields provides a rough proxy for the IMF clock angle, as shown by Brain, Mitchell, et al. (2006). They also showed that accelerated downward-travelling electron spectra (resulting from upward potentials above the MGS spacecraft) are much more common when the clock angle is less than ~240°, indicating a preferential IMF orientation for the acceleration process.

Figure 11 is similar to Figure 10, except that the colors represent two different ranges of IMF clock angle proxy. We observe some marginally significant dependences on clock angle proxy only for low (shallow) elevation

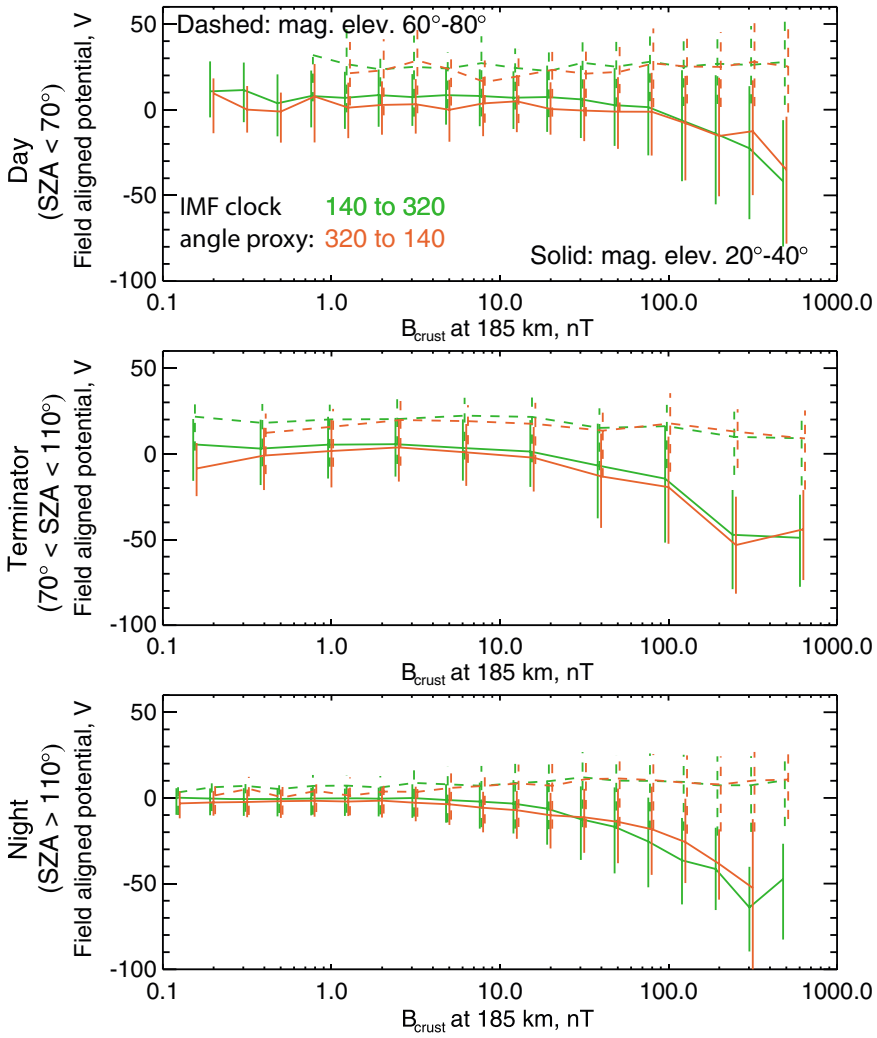

Figure 11. Same as Figure 10 except that the colors represent ranges of interplanetary magnetic field (IMF) clock angle proxy: 140° to 320° (green) and 320° to 140° (orange).

angles. Although these differences are small compared to the interquartile ranges of the data, they are consistent as a function of crustal field strength and therefore may reflect a real dependence. Here we see slightly smaller positive potentials for clock angles 320–140° compared to 140–320°, for all weak crustal field strengths, up to a few tens of nanotesla. This trend is most prominent on the dayside, weaker on the terminator, and very slight on the nightside. Above ~50 nT, there is no clear pattern on the dayside or terminator, but clearly the opposite trend on the nightside, where the "other" IMF direction results in smaller downward field-aligned potentials for shallow elevation angles. A convincing explanation for this dependence, if it is real, would require detailed modeling beyond the scope of this study, as discussed in section 5.3.

5.2.3. Variability With Solar EUV

Solar EUV irradiance drives ionization on the Martian dayside, its intensity linearly determining ionospheric density and hence conductivity. Therefore, we may also expect it to affect field-aligned potentials. However, there was no EUV monitor at Mars before Mars Atmosphere and Volatile Evolution (MAVEN) spacecraft arrived in 2014 (Eparvier et al., 2015). In this absence, EUV measurements made from the Earth's orbit by a series of spacecraft have been used to estimate the full EUV spectrum from 0.1 to 200 nm, which is then scaled and phase-shifted according to solar rotation, to Mars's position via a data assimilation model called FISM-M (Thiemann et al., 2017). We convolve this spectral irradiance with the photoionization cross section of CO_2 (the most common neutral source of ionospheric plasma) and integrate across wavelength to get

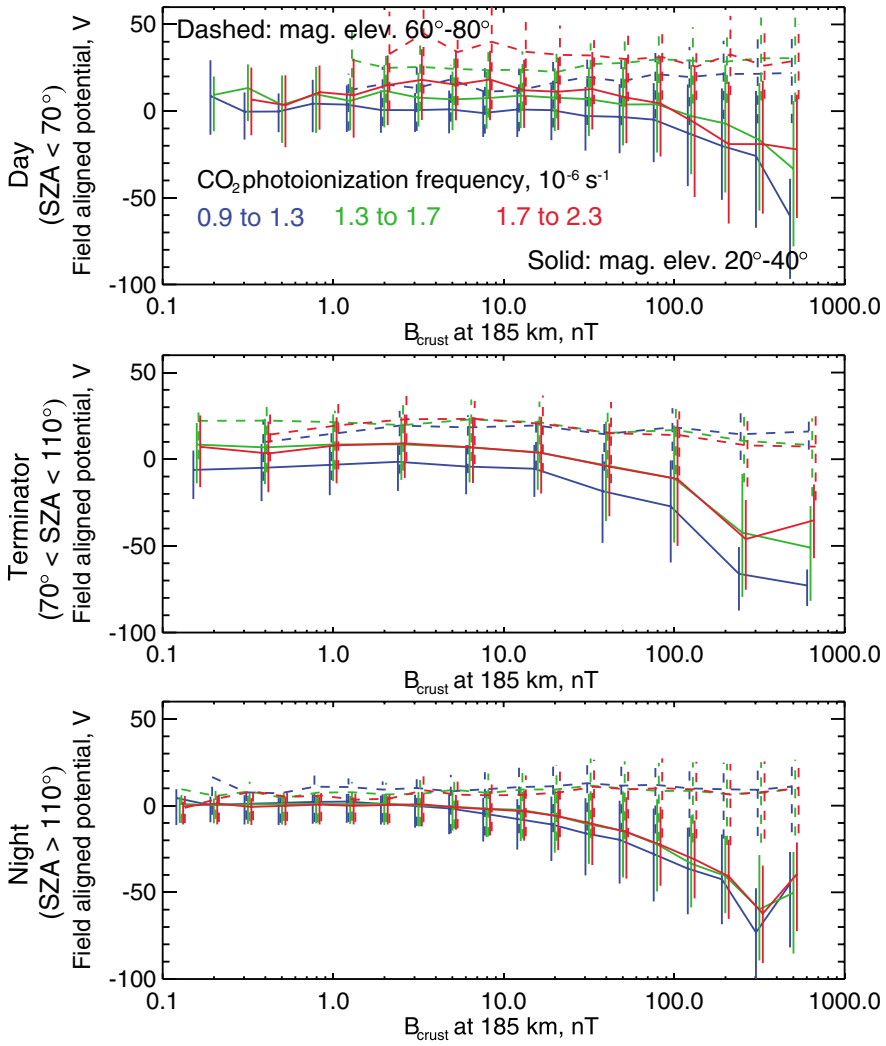

Figure 12. Same as Figure 10 except that the colors represent different ranges of CO_2 photoionization frequency (produced by solar EUV): 0.9–1.3 (pink), 1.3–1.7 (blue), and 1.7–2.3 (red) $\times 10^{-6}$ s^{-1}.

photoionization frequency, that is, the most direct measure of the sun's ability to ionize neutrals at Mars than irradiance in any particular spectral range. The calculation of photoionization frequency is explained in many textbooks and in Appendix A of Lillis et al. (2017).

Figure 12 is similar to Figures 10 and 11, except that the colors represent ranges of CO_2 photoionization frequency. On the dayside, lower solar EUV ($<1.3 \times 10^{-6} s^{-1}$), corresponds to lower positive ΔV for both steep and shallow magnetic elevation angles and weak to moderate crustal field strengths, that is, all magnetic field conditions (and essentially zero ΔV for shallow angles and weak crustal fields). At the terminator, there is no discernible dependence for steep elevation angles (perhaps due to poor statistics), but a similar-to-dayside pattern holds for shallow angles. A simple explanation for this pattern is that higher EUV leads to higher ionospheric densities, meaning higher Pedersen conductivities and hence smaller field-aligned potential drops.

On the nightside where there is no photoionization, as we expect, there is no dependence on EUV for steep angles, no dependence for shallow angles and weak crustal fields, and only a very slight dependence for shallow angles and strong crustal fields, which may reflect the solar wind pressure dependence of Figure 10 as solar activity and perihelion season both tend to see more intense EUV and solar wind together. Indeed, although not shown, a similar pattern to Figure 12 is seen if the data are categorized by inverse square of heliocentric distance.

5.3. Summary of Variables Controlling Field-Aligned Potentials

We observe a hierarchy of the variables controlling the field-aligned potentials that we infer between ~200 km and ~400 km altitude. The strongest determining factor is crustal magnetic field strength. For the weakest crustal magnetic field regions (<~20 nT), diurnal (day-to-night) variability appears to be the most important, with potentials decreasingly positive as one moves from the dayside to the terminator to the nightside. Whereas for the stronger crustal fields (>~20 nT), magnetic elevation angle appears to be the most important determinant of potentials, with shallow angles strongly negative and steep angles moderately positive and this dependence being strongest for the most intense crustal fields.

Beyond these primary correlations, a weaker correlation exists between potentials and solar wind pressure proxy, with stronger negative potentials for lower solar wind pressures, only for strong, shallowly inclined crustal fields. A still weaker correlation exists between potentials and solar EUV on the dayside, with consistently stronger negative potentials for low solar EUV at all crustal field strengths and elevation angles. Lastly, no definitive correlation can be seen with respect to IMF direction proxy.

6. Discussion

In attempting to explain the field-aligned potentials we have derived and analyzed in this study, and their behavior with respect to time of day, crustal magnetic field strength and geometry, and external conditions, it is instructive to look to studies of field-aligned potentials in the Earth's polar cap region, where field lines connect the ionosphere to the earth's dynamic magnetosphere. Here, on a simplistic level, field-aligned conductivities are much higher than perpendicular conductivities in the terrestrial ionosphere, and thus, any potential difference between the magnetosphere and the ionosphere should immediately be neutralized by the mobile electron population at either end of the field line. Thus, consistently measured potential drops have historically been very puzzling, and despite more than four decades of study with increasingly sophisticated modeling and extensive data sets of ground magnetometers, rocket flights, and in situ satellite particle and field measurements, these potential drops are still an active area of research (e.g., Ergun et al., 1998; Marklund et al., 2007).

Thus, given the immature state of research on this topic at Mars, we feel it wiser not to speculate here too deeply as to the causes of the existence or behavior of these potentials. However, given what is known, an explanation likely lies in some combination of the following three aspects of electrodynamics in near-Mars space: (1) magnetospheric plasma flow dynamics and the currents into and out of the ionosphere that are driven as a result, in rough analogy with the earth's polar cap; (2) kinetic plasma effects caused by Mars's unique crustal magnetic fields; and (3) dynamo current systems in the ionosphere. Let us consider these in turn.

First, Dubinin et al. (2008) showed that plasma flow shear in the Martian magnetosheath, in addition to reasonable convection (i.e., nonfield-aligned) electric fields of ~1 mV/m, may be capable of driving field-aligned current densities of up to ~1 $\mu A/m^2$ (which are observed) in the case of auroral electron precipitation. They found that the "inverted V" structures of accelerated electrons indicative of auroral acceleration at earth should occur at Mars and that upward field-aligned potentials of tens to hundreds of volts are required to produce those structures that have indeed been observed by Mars Express and MGS (Brain, Halekas, et al., 2006; Dubinin et al., 2006; Lundin et al., 2006). Plasma flow shear can be caused by the passage of solar wind structures such as stream interaction regions (i.e., the interface between fast and slow solar wind streams; e.g., Gosling et al., 1978) or coronal mass ejections, or by turbulence in the Martian plasma environment (e.g., Ruhunusiri et al., 2017) or by Kelvin Helmholtz instabilities at the boundary between the Martian magnetosheath and magnetic pileup region (Ruhunusiri et al., 2016). In addition, so-called double layers of opposite electric charge could help to maintain parallel potentials, as has been inferred from observations in the Earth's auroral zone (Mozer & Kletzing, 1998). This broad range of possible sources may explain some of the variability in our derived electrostatic potentials.

Second, Mars's highly inhomogeneous crustal magnetic fields make the situation markedly different from the terrestrial one. The geometry of individual crustal magnetic anomalies results in mini-magnetospheres with open and closed field regions, with different orientations and sizes resulting

from different distributions and strengths of subsurface crustal magnetization. Not only are each of these mini-magnetospheres different, they are in many cases close enough to one another to substantially affect the electrodynamics of each other. Further, large swaths of the planet (e.g., Tharsis) are completely devoid of crustal magnetic fields, leading to a primarily Venus-like interaction of the ionosphere with the draped interplanetary magnetic field (e.g., Nagy et al., 2004). Each of these different geometries is expected to lead to a different kind of typical current system on the dayside, nightside, and at the terminator. In addition, the crustal magnetic fields themselves are hundreds to thousands of times weaker than Earth's global dipole field at ionospheric altitudes. Therefore, while electrons have gyroradii of a few kilometers at most and therefore typically bound to magnetic field lines at all energies where substantial electron flux exists, ion gyroradii are larger by a factor of $\sqrt{(m_i/m_e)}$, where m_i and m_e are the masses of ions and electron, respectively. The two most common planetary ions in near-Mars space, O^+ and O_2^+, thus have gyroradii 172 and 243 times larger than electrons, respectively. Depending on magnetic geometry and topology, this can lead to charge separations and resulting electrostatic potentials, both within the photochemically dominated ionosphere and the collisionless region above.

Third and last, the current systems that link the Martian ionosphere and magnetosphere must close through the ionosphere and are therefore affected by, and must be consistent with, ionospheric dynamo current systems driven by thermospheric winds and magnetic gradient and curvature drifts. Mittelholz et al. (2017) found a global-scale pattern of external (i.e., noncrustal) current-produced magnetic fields at ~400 km quite similar to that of predicted thermospheric winds, similar to the Sq (solar quiet) current on Earth, strongly suggesting the influence of neutral winds on ionospheric currents at Mars. Riousset et al. (2013) modeled these current systems at high resolution near an idealized crustal magnetic dipole and multi-dipole arcade for the simplest case of uniform horizontal neutral winds. They found a rich and complex current structure, even for the simplistic case of a spatially uniform, unchanging wind velocity.

In reality, the vertical distribution of ionospheric currents will depend on the altitude profile of Pedersen and Hall conductivity and the degree to which wind-driven currents and electrojets (Fillingim et al., 2012; Opgenoorth et al., 2010) are shielded from, or couple with, currents originating in a higher altitude collisionless plasma flows.

These three aforementioned aspects of electrodynamics in near-Mars space are likely responsible, in various combinations under different conditions, for the patterns and variability in field-aligned potentials we observe.

7. Summary

We have presented a study of electrostatic potential differences along magnetic field lines between ~400 km and ~180 km above Mars, derived from the shapes of suprathermal electron loss cones measured by Mars Global Surveyor at 370–430 km altitude at 2 A.M. and 2 P.M. local time. We find that potentials are stronger in regions of stronger crustal magnetic fields and that an average structure exists whereby potentials are generally positive near the center of topologically open crustal fields where field lines are steeper and generally negative near the edges of such regions near the boundaries with closed magnetic fields, where fields are shallower. This structure may be due to charge separations resulting from magnetospheric plasma flow and kinetic effects in Mars's substantial but (compared to Earth) weak magnetic fields, whereby electrons and ions are strongly and weakly magnetized, respectively. This underlying structure is less pronounced for the dayside compared to nightside and for higher solar wind pressures and (on the dayside) higher solar EUV irradiances.

While this study benefited from an extremely large data set at a consistent altitude and local time, the next step in understanding Mars's extremely rich electrodynamic environment is to use data from the MAVEN spacecraft (Jakosky et al., 2015), which is collected over a much larger range of altitudes (150–6,000 km) and a wide variety of local times. This allows much more accurate individual measurements of electrostatic potential differences due to a full suite of plasma instruments and a carefully controlled and monitored spacecraft potential. In particular, this will allow us to probe the vertical structure of these potentials, understand their consequences (e.g., aurora, ionization, and heating), and elucidate the processes responsible for their formation and variability.

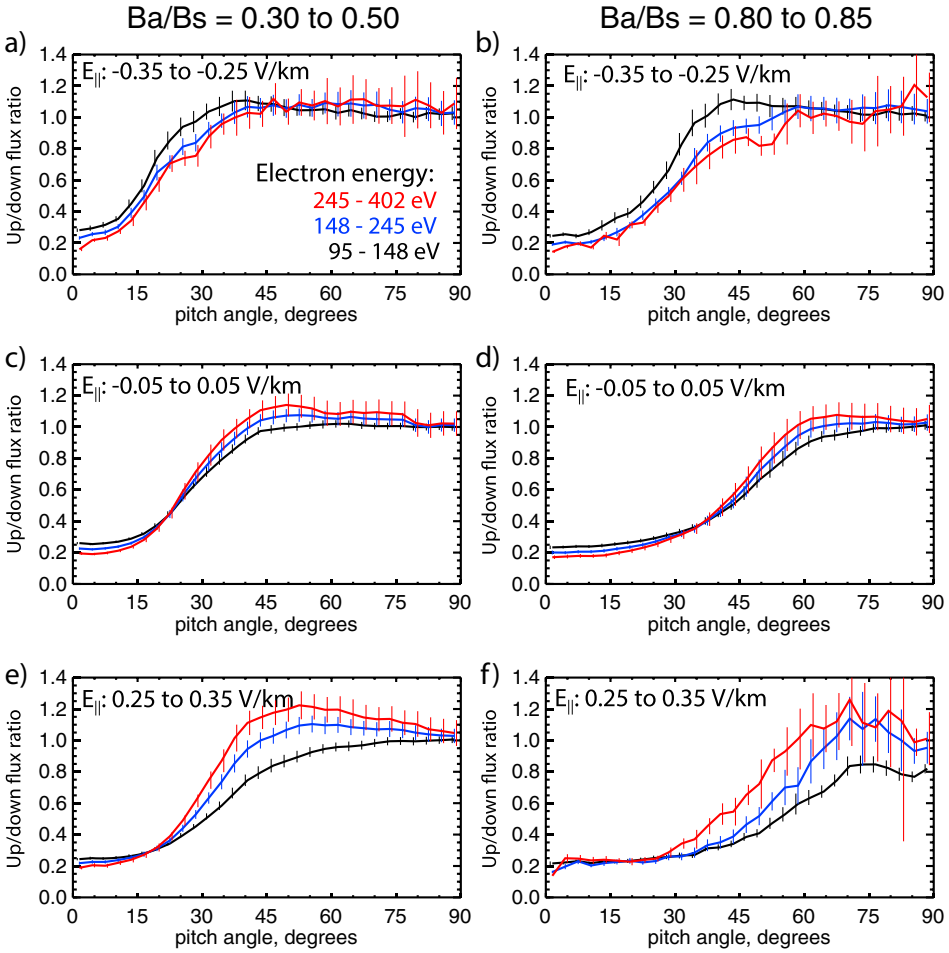

Figure A1. Pitch angle distributions in three adjacent energy channels (95–148 eV in black, 148–245 eV in blue, and 245–402 eV in red) are shown as ratios of upward flux at pitch angle α to downward flux at the conjugate pitch angle of $180° - \alpha$. In particular, shown are the mean and standard deviations of this ratio in three degree pitch angle bins for all measured PADs whose best-fit values for $E_{||}$ and B_a/B_s fall into the same range. (top row) Significant negative (downward), (middle row) approximately zero, and (bottom row) significantly positive (upward) potentials. (left column) Cases of moderate to strong crustal field, where the ratio B_a/B_s of noncrustal to total magnetic field at the spacecraft is between 0.30 and 0.50. (right column) Cases of weak-to-moderate crustal fields where B_a/B_s is between 0.80 and 0.85.

Appendix A: Validation of the Fitting Procedure

Because the uncertainties in any single derivation of $E_{||}$ are typically large, we wish to provide a statistically significant demonstration that our fitting procedure (including the backscatter subtraction step) is indeed capable of estimating field-aligned potentials. If so, we should see a clear, intuitively understandable energy-dependent pattern in the loss cone shapes for similar derived values of B_a/B_s and $E_{||}$. Therefore, let us examine raw, unbackscatter-subtracted ratios of upward to downward fluxes as a function of pitch angle and energy, averaged over all PADs in the data set that have a similar range of best fit values of B_a/B_s and $E_{||}$.

This is shown in Figure A1. The left column shows cases of moderate to strong crustal field, where the best-fit ratio B_a/B_s of noncrustal to crustal magnetic field at the spacecraft is between 0.30 and 0.50. The right column shows cases of weak-to-moderate crustal fields where B_a/B_s is between 0.80 and 0.85. The top row shows cases where significant negative potentials are the best fit and where, as expected, we see higher fluxes in the decreasing-flux part of the loss cone for lower energies because the potential exerts a greater proportional upward force on these electrons compared to higher energies; that is, the total potential drop between the spacecraft and the magnetic reflection altitude is a greater fraction of their total energy. The opposite is true for the bottom row of Figure A1, which shows cases of significant positive potentials, where we see lower

fluxes in the loss cone for lower energies because the potential exerts a greater proportional downward force on these electrons compared to higher energies. The middle row of Figure A1 shows cases where the derived potential is on average zero, that is, the shapes are determined by the magnetic mirror force and by atmospheric scattering alone. Here we see that, as expected, the loss cones are steeper at higher energies because the atmosphere is a more efficient absorber due to smaller-angle scattering for elastic collisions (e.g., Figure 4 of Lillis & Fang, 2015) and, also as expected for a lack of field-aligned potentials, there is no significant energy-dependent shift of the loss cone. Thus, we see that the average loss cone shapes measured by MAG/ER are intuitively consistent with the potentials derived for those loss cones.

However, it is worth mentioning a caveat here. For many of the derived positive potentials, Figure A1e shows that the 245–402 eV electrons (red lines), and to a lesser extent the 148–245 eV electrons (blue lines), are somewhat enhanced over their downward counterparts (i.e., the up/down flux ratio is >1). The further from 90°, the larger the enhancement, reaching ~10–20% just before the loss cone begins at around 50° pitch angle. However, the 95–148 eV electrons (black lines) appear to be depleted, in a way that is consistent with being sucked down into the atmosphere by a positive electrostatic potential or by being accelerated to higher energies without being replaced by energization of lower energy electrons. However, given the typical falling spectrum of sheath and tail electrons measured by MGS whereby 95–148 eV electron fluxes are approximately three to four times higher than 245–402 eV fluxes (Mitchell et al., 2001), only ~20–30% of the depletion of upward-traveling 95–148 eV electrons can by itself explain the increase in 148–245 and 245–402 eV electrons, the remainder presumably being due to positive potentials. Thus, it is conceivable that some mechanism acting on the precipitating electrons, perhaps resonant wave heating, may at times be preferentially heating ~100 eV (but not lower energy) electrons to higher energies and thus partially masking the signature of some positive electrostatic potentials in situations with moderate-to-strong crustal magnetic fields such as that shown in Figure A1e. Note that the loss cones in Figure A1f are more obviously shifted with respect to each other, thus indicating a lower or negligible masking. In other words, our technique may at times be somewhat overestimating positive potentials.

Appendix B: Correcting for Biased Values of $E_{||}$

B1. Limitations Imposed by Loss Cone Formation

As well as the uncertainties in the derived values of $E_{||}$ discussed in section 3.2, our ability to constrain the field-aligned potential is also limited by the physics of loss cone formation. If we treat the atmosphere as a perfect absorber, the loss cone angle is the pitch angle furthest from 90° at which downward-traveling electrons can magnetically reflect back upward before being absorbed by the collisional atmosphere. In the real case of a "fuzzy" atmospheric barrier, we can think of the loss cone angle as the pitch angle at which the returning flux is reduced by, say, 50% (e.g., 23° in Figure A1c). As mentioned earlier, our fitting technique relies on being able to measure how the loss cone shifts in angle for different energies; that is, we must be able to resolve the loss cone angle in at least two of our three reliable energy channels.

However, if the field-aligned potential below the spacecraft is too strongly positive (upward), then the negatively charged electrons at all pitch angles will be pulled downward into the collisional atmosphere, and none will magnetically reflect back upward to provide a measure of the loss cone angle; that is, the loss cone will form at 90°. The weaker the magnetic mirror force, the smaller the positive potential that is required for this to occur.

Conversely, in the rare case that the potential is both negative (i.e., downward) and more than ~250 V, then electrons at all pitch angles in the 95–148 and 148–245 eV channels will be pushed upward, that is, electrostatically reflected, before encountering any substantial atmosphere, and the upward flux will mirror the downward flux, with no loss cone forming at all.

This means that, for a given value of B_a/B_s, there is a maximum and minimum theoretical value of $E_{||}$ that can be detected using our method. So in cases where the field-aligned electric field exceeds these theoretical maximum or minimum values, the loss cone cannot be measured, and the method does not return any derived value of $E_{||}$. Figure B1 shows the same type of data as in Figure A1 (i.e., up/down flux ratios as a function of pitch angle) but for a broad range of derived values of B_a/B_s and $E_{||}$, placed alongside loss cone shapes simulated using our adiabatic model for the same values of B_a/B_s. We can clearly see that as B_a/B_s approaches

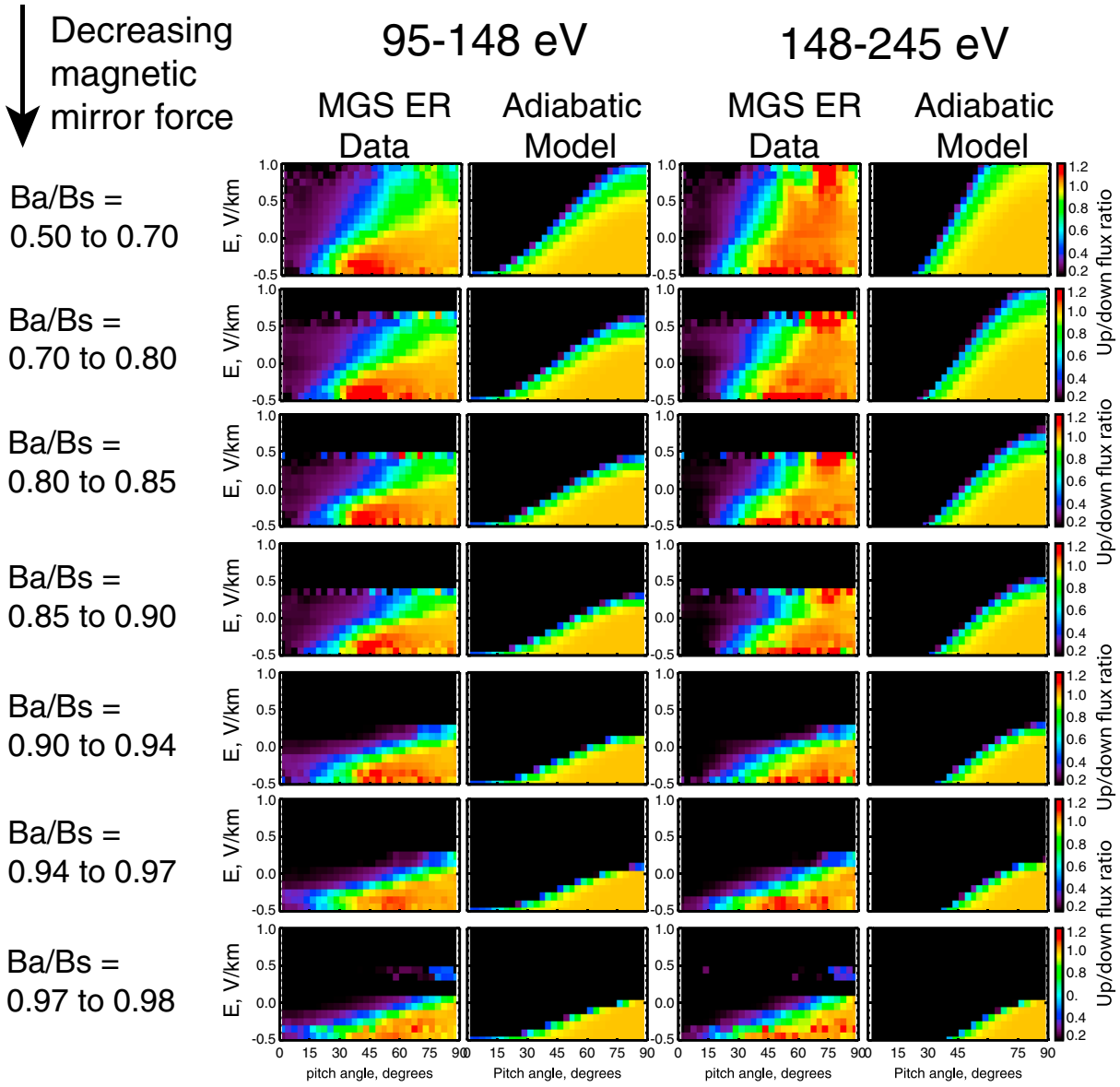

Figure B1. The range of derivable values of $E_{||}$ is limited by the physics of loss cone formation. (first and third columns) The averages of all normalized measured pitch angle distributions for which the derived values of B_a/B_s and $E_{||}$ are as shown by the labels on the left and on the *y* axes of each panel (e.g., the bottom row of colors in the top left panel shows the average ratio of the upward to downward fluxes for 90–145 eV electrons in cases where the fitting procedure results in values of B_a/B_s between 0.5 and 0.7 and values of $E_{||}$ between −0.5 and −0.4). (second and fourth columns) The results of the adiabatic model (i.e., excluding atmospheric backscatter) of the loss cone formation discussed in sections 3.1 and 3.2, for the same values of energy, B_a/B_s and $E_{||}$.

1.0 (i.e., as the magnetic mirror force weakens toward zero), a progressively narrower range of positive electrostatic potentials can be derived, until at B_a/B_s = 1 (i.e., no magnetic mirror force), no positive potentials may be derived at all. We show the adiabatic model results not because we expect them to match the data precisely (e.g., the model does not simulate atmospheric backscatter, and so the loss cones appear sharper than reality) but as another check that our fitting technique gives reasonable results for $E_{||}$.

Thus, when we examine mean values of $E_{||}$ collected under similar sets of conditions (i.e., season, geography, local time, etc.), we must be aware of the bias in the data that results from this limitation and how it may affect those mean values we would like to interpret. Of course, we cannot know for sure the distribution of the missing values of $E_{||}$, but with some reasonable assumptions, we can correct for this bias insofar as

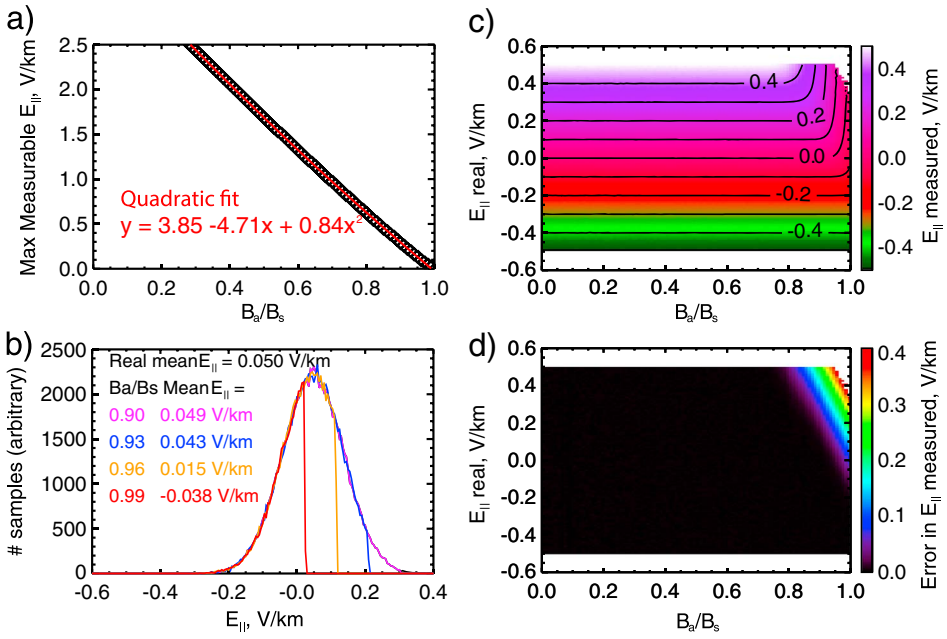

Figure B2. Bias in the retrieval technique for $E_{||}$. (a) The maximum value of $E_{||}$ (black diamonds) that can be derived using our method, as a function of B_a/B_s, and a quadratic fit to those values (red line). (b) A theoretical distribution of values of $E_{||}$ and how it is truncated to worsening degrees for higher values of B_a/B_s (i.e., weaker magnetic mirror forces). (c) How measured mean values of $E_{||}$ are affected by this truncation is shown, and (d) the resulting error in these mean values is shown, concentrated where $E_{||}$ is positive and B_a/B_s is >~0.8.

possible. We now present two methods of correction, along with their assumptions. The first is simple, the second more involved; the results they give are quite similar to one another.

B2. Simple Method of Correcting Values of $E_{||}$

Let us first examine the part of the parameter space defined by $E_{||}$ and B_a/B_s where this bias occurs. Figure B2a shows the maximum measurable value of $E_{||}$ as a function of B_a/B_s according to our adiabatic loss cone model (see Figure B1) and a quadratic fit to it, while Figure B2b demonstrates how a theoretical distribution of values of $E_{||}$ would be truncated by this limitation. In order to estimate what effect this bias has on mean values of $E_{||}$ from truncated distributions, we fitted Gaussian curves to the measured distributions of $E_{||}$ for each 0.01 increment of B_a/B_s. We used the widths of these measured distributions to create theoretical distributions for mean values of $E_{||}$ between −0.5 and +0.5 V/km, then truncated these theoretical distributions according to the curve in Figure B2a and calculated the resulting "biased" means (Figure B2c) and the difference between them and the "real" mean (Figure B2d). In other words, we calculated the amount by which we would underestimate (i.e., bias negatively) mean values of $E_{||}$ from symmetric distributions due to truncation, like that shown in Figure B2b. We see clearly that the bias region is triangular in shape in the upper right of the parameter space and that the bias is worse for more positive values of $E_{||}$ and larger values of B_a/B_s (i.e., weaker magnetic mirror forces).

Figure B2 is instructive in showing how the bias manifests itself and where the problem area lies. It also provides a simplistic method of correcting individual values of $E_{||}$ under the assumption that the "real" values are normally and symmetrically distributed in $E_{||}$; that is, for each data point, take the measured value of B_a/B_s (i.e., along the *x* axis in Figure B2b), and find the "real" value of $E_{||}$ that corresponds to the measured value of $E_{||}$ (i.e., move upward from the *x* axis to the contour with that measured value, and read off the *y* axis).

B3. Kolmogorov–Smirnov Correction Method

However, we can also employ a method that uses the real distribution of values of $E_{||}$ within a given subset of the data for which we wish to estimate the most likely mean and the degree to which the bias has affected it. Here we rely on the fact that a truncated distribution can reliably be distinguished from a symmetric distribution using the classic Kolmogorov–Smirnov (KS) test; that is, for a given range of values of B_a/B_s, we can

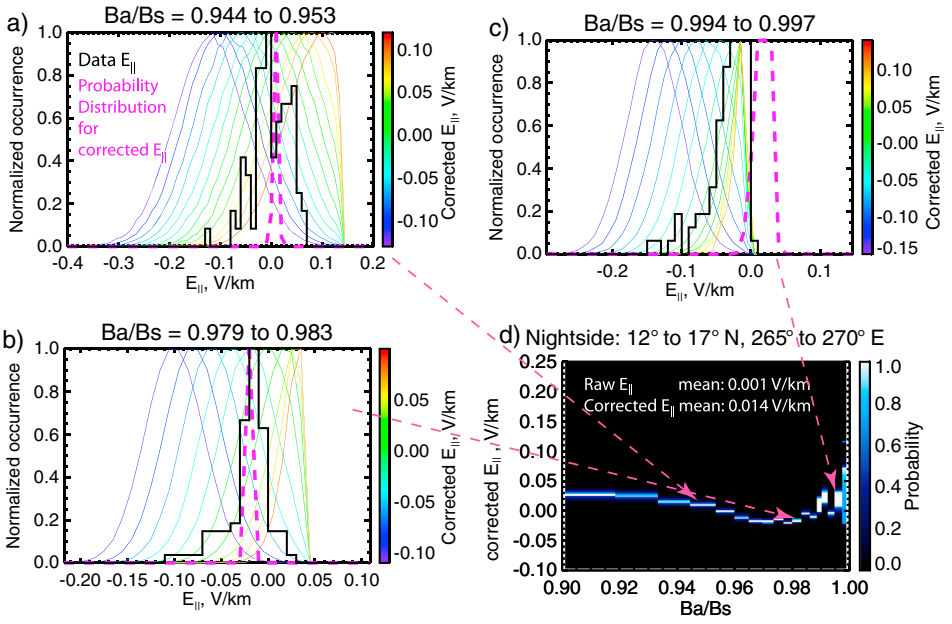

Figure B3. Example of correction of mean values of $E_{||}$. A total of 1,963 derived values of $E_{||}$ were measured on the nightside of Mars in a small geographic box in the Tharsis region (very weak crustal fields): 12°–17°N, 265°–270°E. (a–c) Three example ranges of B_a/B_s, each with 93 data points. The black histogram bars represent the derived values of $E_{||}$, that is, the data. The thin colored lines show theoretical probability distributions for different "real" mean values of $E_{||}$, truncated according to the curve in Figure 15a, and colored according to the color bar. The dashed pink lines show the normalized Kolmogorov–Smirnov probability that the data are drawn from the same distribution as the truncated theoretical curves, as a function of the corrected mean value of $E_{||}$ corresponding to each curve. Only Figure 16c shows a corrected value substantially different from a straightforward mean. (d) Probability distributions in corrected $E_{||}$ for each of the 19 ranges of B_a/B_s.

calculate the relative likelihood that our measured distribution of $E_{||}$ values came from various parent distributions, including truncated distributions.

For any collection of data points for which we would like to calculate a mean value of $E_{||}$, we first divide up the data into separate ranges of B_a/B_s, ensuring that we have at least 30 data points for each range to ensure sufficient statistics. Then for each range of B_a/B_s, we calculate theoretical expected distributions of $E_{||}$ for a wide range of "real" values of $E_{||}$ (from −1.5 V/km to 1.5 V/km), that is, truncated where appropriate according to the maximum measurable $E_{||}$ curve in Figure B2a. Every theoretical distribution in each B_a/B_s range has a width in $E_{||}$ consistent with the overall data set. We then apply the KS test to calculate the probability that the measured distribution of $E_{||}$ values (i.e., data) came from the same parent distribution as each of our theoretical distributions of $E_{||}$. Since each of those distributions corresponds to a "real" mean value of $E_{||}$, we thus calculate a probability distribution for the "corrected" mean value of $E_{||}$, that is, the mean we would have calculated if it were not for the aforementioned bias. We consider the mean value of this distribution to be the corrected value for this range of B_a/B_s. We then calculate an overall corrected mean, weighted by the number of data points in each B_a/B_s range.

Figure B3 shows an example of this method for a set of ~2,000 data points collected on the nightside over a small 5° × 5° box in the Tharsis region, where crustal fields are extremely weak (0.74 nT mean at 185 km; Lillis, Dufek, et al., 2009), illustrating the relationship between the measured and theoretical distributions for various values of the "real" (i.e., corrected) values of $E_{||}$. Figure B3a shows a range of B_a/B_s (0.944 to 0.953) where none of the measured values of $E_{||}$ come particularly too close to the maximum measurable value of 0.14 V/km, so none of the significantly truncated theoretical distributions fit the data very well and the highest KS probabilities are for values of $E_{||}$ between 0 and 0.01 V/km. Figure B3b shows a higher range of B_a/B_s (0.979 to 0.983) where the bias problem is worse; however, the measured values of $E_{||}$ are mostly negative, with none getting too close to the maximum measurable value of 0.045 V/km. We should note that it is of course possible that we are missing a separate population of substantially more positive values of $E_{||}$ that fall above the maximum measurable value. However,

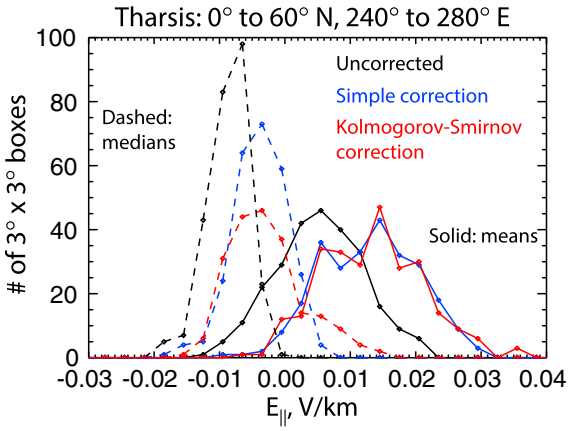

Figure B4. Comparison of histograms of mean (solid lines) and median (dashed lines) values of $E_{||}$ in each 3° × 3° geographic box in a large swath of the Tharsis region where crustal magnetic fields are extremely weak. Three calculation methods are shown: means of values of $E_{||}$ (black), means of values of $E_{||}$ corrected using the simple correction method described in Appendix B2 (blue), and means calculated using the Kolmogorov–Smirnov method described in Appendix B3 (red).

if there were a substantial population at these higher positive field values, it seems unlikely that over the whole data set, there would be no values close to the maximum. In any case, it is impossible to quantify this source of uncertainty, so we shall employ Occam's razor and ignore it.

Figure B3c shows a case where our correction technique makes a difference. In this case, the data distribution appears truncated, and hence, the truncated theoretical distributions with corrected values of $E_{||}$ somewhat above the maximum value give the highest KS probabilities. Figure B3d shows "corrected $E_{||}$" probabilitydistributions for 18 ranges of B_a/B_s above 0.9 (>90% of data points in this case), with 93 data points in each range. This shows that (a) there appears to be a real correlation between $E_{||}$ and B_a/B_s for this set of data points and that(b) in this case the overall mean value was corrected from essentially zero to 0.014 V/km, or about ~3 V between the spacecraft (~400 km) and the electron absorption region (~200 km).

B4. Comparison of Correction Methods

The simple correction method can be applied to any data point, since we always derive a pair of values of B_a/B_s and $E_{||}$. The Kolmogorov–Smirnov method calculates mean values of $E_{||}$ where we have a sufficient number of data points (~50 or more) to make the KS probabilities meaningful. Let us now compare these methods within 3° × 3° boxes over a 40° longitude × 60° latitude swath of the Tharsis volcanic region where the crustal field (i.e., magnetic mirror force) is very weak and hence B_a/B_s is often large enough for the correction to be nonnegligible (52% of values of B_a/B_s in the data set are above 0.97). Figure B4 shows this comparison, for both means and medians. First, we see that both the simple and KS methods shift the distribution positive by ~0.01 V/km. This may not seem like a large amount, but it is ~2.2 V over the distance between the spacecraft and the collisional atmosphere, a substantial fraction of the ~10 V ambipolar potential seen in the ionosphere of Venus (Collinson et al., 2016). Second, and importantly, both correction methods give very similar distributions of values of $E_{||}$, especially for means. Therefore, we choose to apply the simple correction to the entire data set of values of $E_{||}$.

Acknowledgments
The data used in this manuscript (magnetic field and electron pitch angle measurements from Mars Global Surveyor MAG/ER) may be accessed at https://pds.nasa.gov/ds-view/pds/viewDataset.jsp?dsid=MGS-M-ER-4-MAP1%2FANGULAR-FLUX-V1.0. The processed data set of derived electrostatic potentials may be found, in the form of ASCII table files, in the supporting information.

References

Acuña, M. H., Connerney, J. E. P., Wasilewski, P., Lin, R. P., Mitchell, D., Anderson, K. A., … Ness, N. F. (2001). Magnetic field of Mars: Summary of results from the aerobraking and mapping orbits. *Journal of Geophysical Research*, *106*, 23,403–23,417. https://doi.org/10.1029/2000JE001404

Bertaux, J. L., Leblanc, F., Witasse, O., Quemerais, E., Lilensten, J., Stern, S. A., … Korablev, O. (2005). Discovery of an aurora on Mars. *Nature*, *435*(7043), 790–794. https://doi.org/10.1038/nature03603

Bevington, P. R., & Robinson, D. K. (2003). *Data reduction and error analysis for the physical sciences* (3rd ed., Vol. xi, p. 320). Boston, MA: McGraw-Hill.

Brain, D. A. (2005). Variability of the altitude of the Martian sheath. *Geophysical Research Letters*, *32*, L18203. https://doi.org/10.1029/2005GL023126

Brain, D. A. (2007). Mars Global Surveyor measurements of the Martian solar wind interaction. *Space Science Reviews*, *126*(1-4), 77–112. https://doi.org/10.1007/s11214-006-9122-x

Brain, D. A., Halekas, J. S., Peticolas, L. M., Lin, R. P., Luhmann, J. G., Mitchell, D. L., … Reme, H. (2006). On the origin of aurorae on Mars. *Geophysical Research Letters*, *33*, L01201. https://doi.org/10.1029/2005GL024782

Brain, D. A., Lillis, R. J., Mitchell, D. L., Halekas, J. S., & Lin, R. P. (2007). Electron pitch angle distributions as indicators of magnetic field topology near Mars. *Journal of Geophysical Research*, *112*, A09201. https://doi.org/10.1029/2007JA012435

Brain, D. A., Mitchell, D. L., & Halekas, J. S. (2006). The magnetic field draping direction at Mars from April 1999 through August 2004. *Icarus*, *182*(2), 464–473. https://doi.org/10.1016/j.icarus.2005.09.023

Collinson, G. A., Frahm, R. A., Glocer, A., Coates, A. J., Grebowsky, J. M., Barabash, S., … Zhang, T. L. (2016). The electric wind of Venus: A global and persistent "polar wind"-like ambipolar electric field sufficient for the direct escape of heavy ionospheric ions. *Geophysical Research Letters*, *43*, 5926–5934. https://doi.org/10.1002/2016GL068327

Crider, D. H. (2003). A proxy for determining solar wind dynamic pressure at Mars using Mars Global Surveyor data. *Journal of Geophysical Research*, *108*(A12), 1461. https://doi.org/10.1029/2003JA009875

Diéval, C., Stenberg, G., Nilsson, H., & Barabash, S. (2013). A statistical study of proton precipitation onto the Martian upper atmosphere: Mars Express observations. *Journal of Geophysical Research: Space Physics*, *118*, 1972–1983. https://doi.org/10.1002/jgra.50229

Dubinin, E., Chanteur, G., Fraenz, M., & Woch, J. (2008). Field-aligned currents and parallel electric field potential drops at Mars. Scaling from the Earth' aurora. *Planetary and Space Science*, *56*(6), 868–872. https://doi.org/10.1016/j.pss.2007.01.019

Dubinin, E., Lundin, R., Fränz, M., Woch, J., Barabash, S., Fedorov, A., … Carter, M. (2006). Electric fields within the martian magnetosphere and ion extraction: ASPERA-3 observations. *Icarus*, *182*(2), 337–342. https://doi.org/10.1016/j.icarus.2005.05.022

Eastwood, J. P., Brain, D. A., Halekas, J. S., Drake, J. F., Phan, T. D., Øieroset, M., … Acuña, M. (2008). Evidence for collisionless magnetic reconnection at Mars. *Geophysical Research Letters*, *35*, L02106. https://doi.org/10.1029/2007GL032289

Edberg, N. J. T., Lester, M., Cowley, S. W. H., & Eriksson, A. I. (2008). Statistical analysis of the location of the Martian magnetic pileup boundary and bow shock and the influence of crustal magnetic fields. *Journal of Geophysical Research*, *113*, A0820. https://doi.org/10.1029/2008JA013096

Eparvier, F., Chamberlin, P. C., & Woods, T. N. (2015). The solar extreme ultraviolet monitor for MAVEN. *Space Science Reviews*, *195*(1-4), 293–301. https://doi.org/10.1007/s11214-015-0195-2

Ergun, R. E., Carlson, C. W., McFadden, J. P., Mozer, F. S., Delory, G. T., Peria, W., … Kistler, L. (1998). FAST satellite observations of electric field structures in the auroral zone. *Geophysical Research Letters*, *25*, 2025–2028. https://doi.org/10.1029/98GL00635

Fillingim, M. O., Lillis, R. J., England, S. L., Peticolas, L. M., Brain, D. A., Halekas, J. S., … Bougher, S. W. (2012). On wind-driven electrojets at magnetic cusps in the nightside ionosphere of Mars. *Earth, Planets and Space*, *64*(2), 93–103. https://doi.org/10.5047/eps.2011.04.010

Fillingim, M. O., Peticolas, L. M., Lillis, R. J., Brain, D. A., Halekas, J. S., Lummerzheim, D., & Bougher, S. W. (2010). Localized ionization patches in the nighttime ionosphere of Mars and their electrodynamic consequences. *Icarus*, *206*(1), 112–119. https://doi.org/10.1016/j.icarus.2009.03.005

Gosling, J. T., Asbridge, J. R., Bame, S. J., & Feldman, W. C. (1978). Solar wind stream interfaces. *Journal of Geophysical Research*, *83*, 1401–1412. https://doi.org/10.1029/JA083iA04p01401

Halekas, J. S., Brain, D., Lin, R. P., Luhmann, J., & Mitchell, D. L. (2007). Distribution and variability of accelerated electrons at Mars. *Advances in Space Research*, *41*, 1347–1352. https://doi.org/10.1016/j.asr.2007.01.034

Halekas, J. S., & Brain, D. A. (2010). Global distribution, structure, and solar wind control of low altitude current sheets at Mars. *Icarus*, *206*(1), 64–73. https://doi.org/10.1016/j.icarus.2008.12.032

Halekas, J. S., Brain, D. A., Lillis, R. J., Fillingim, M. O., Mitchell, D. L., & Lin, R. P. (2006). Current sheets at low altitudes in the Martian magnetotail. *Geophysical Research Letters*, *33*, L13101. https://doi.org/10.1029/2006GL026229

Halekas, J. S., Delory, G. T., Lin, R. P., Stubbs, T. J., & Farrell, W. M. (2008). Lunar Prospector observations of the electrostatic potential of the lunar surface and its response to incident currents. *Journal of Geophysical Research*, *113*, A09102. https://doi.org/10.1029/2008JA013194

Halekas, J. S., Lillis, R. J., Mitchell, D. L., Cravens, T. E., Mazelle, C., Connerney, J. E. P., … Ruhunusiri, S. (2015). MAVEN observations of solar wind hydrogen deposition in the atmosphere of Mars. *Geophysical Research Letters*, *42*, 8901–8909. https://doi.org/10.1002/2015GL064693

Halekas, J. S., Lin, R. P., & Mitchell, D. L. (2005). Large negative lunar surface potentials in sunlight and shadow. *Geophysical Research Letters*, *32*, L09102. https://doi.org/10.1029/2005GL022627

Hara, T., Luhmann, J. G., Leblanc, F., Curry, S. M., Seki, K., Brain, D. A., … Jakosky, B. M. (2017). MAVEN observations on a hemispheric asymmetry of precipitating ions toward the Martian upper atmosphere according to the upstream solar wind electric field. *Journal of Geophysical Research: Space Physics*, *122*, 1083–1101. https://doi.org/10.1002/2016JA023348

Hara, T., Seki, K., Futaana, Y., Yamauchi, M., Barabash, S., Fedorov, A. O., … Delcourt, D. C. (2013). Statistical properties of planetary heavy-ion precipitations toward the Martian ionosphere obtained from Mars Express. *Journal of Geophysical Research: Space Physics*, *118*, 5348–5357. https://doi.org/10.1002/jgra.50494

Harada, Y., Halekas, J. S., McFadden, J. P., Mitchell, D. L., Mazelle, C., Connerney, J. E. P., … Jakosky, B. M. (2015). Magnetic reconnection in the near-Mars magnetotail: MAVEN observations. *Geophysical Research Letters*, *42*, 8838–8845. https://doi.org/10.1002/2015GL065004

Jakosky, B. M., Lin, R. P., Grebowsky, J. M., Luhmann, J. G., Mitchell, D. F., Beutelschies, G., … Zurek, R. (2015). The Mars Atmosphere and Volatile Evolution (MAVEN) mission. *Space Science Reviews*, *195*(1-4), 3–48. https://doi.org/10.1007/s11214-015-0139-x

Kallio, E., & Barabash, S. (2001). Atmospheric effects of precipitating energetic hydrogen atoms on the Martian atmosphere. *Journal of Geophysical Research*, *106*, 165–177. https://doi.org/10.1029/2000JA002003

Leblanc, F., Luhmann, J., Johnson, R. E., & Chassefiere, E. (2002). Some expected impacts of a solar energetic particle event at Mars. *Journal of Geophysical Research*, *107*(A5), 1058. https://doi.org/10.1029/2001JA900178

Leblanc, F., Modolo, R., Curry, S., Luhmann, J., Lillis, R., Chaufray, J. Y., … Jakosky, B. (2015). Mars heavy ion precipitating flux as measured by Mars Atmosphere and Volatile EvolutioN. *Geophysical Research Letters*, *42*, 9135–9141. https://doi.org/10.1002/2015GL066170

Leblanc, F., Witasse, O., Lilensten, J., Frahm, R. A., Safaenili, A., Brain, D. A., … Lundin, R. (2008). Observations of aurorae by SPICAM ultraviolet spectrograph on board Mars Express: Simultaneous ASPERA-3 and MARSIS measurements. *Journal of Geophysical Research*, *113*, A08311. https://doi.org/10.1029/2008JA013033

Lillis, R. J., Bougher, S. W., Mitchell, D. L., Brain, D. A., Lin, R. P., & Acuna, M. H. (2008). Continuous monitoring of nightside upper thermospheric mass densities in the Martian southern hemisphere over 4 Martian years using electron reflectometry. *Icarus*, *194*(2), 562–574. https://doi.org/10.1016/j.icarus.2007.09.031

Lillis, R. J., & Brain, D. A. (2013). Nightside electron precipitation at Mars: Geographic variability and dependence on solar wind conditions. *Journal of Geophysical Research: Space Physics*, *118*, 3546–3556. https://doi.org/10.1002/Jgra.50171

Lillis, R. J., Deighan, J., & Fox, J. (2017). Photochemical escape of oxygen from Mars: First results from MAVEN in situ data. *Journal of Geophysical Research: Space Physics*, *122*, 3815–3836. https://doi.org/10.1002/2016JA023525

Lillis, R. J., Dufek, J., Bleacher, J. E., & Manga, M. (2009). Demagnetization of crust by magmatic intrusion near the Arsia Mons volcano: Magnetic and thermal implications for the development of the Tharsis province, Mars. *Journal of Volcanology and Geothermal Research*, *185*(1-2), 123–138. https://doi.org/10.1016/j.jvolgeores.2008.12.007

Lillis, R. J., Dufek, J., Kiefer, W. S., Black, B. A., Manga, M., Richardson, J. A., & Bleacher, J. E. (2015). The Syrtis Major volcano, Mars: A multidisciplinary approach to interpreting its magmatic evolution and structural development. *Journal of Geophysical Research: Planets*, *120*, 1476–1496. https://doi.org/10.1002/2014JE004774

Lillis, R. J., & Fang, X. (2015). Electron impact ionization in the Martian atmosphere: Interplay between scattering and crustal magnetic field effects. *Journal of Geophysical Research: Planets*, *120*, 1332–1345. https://doi.org/10.1002/2015JE004841

Lillis, R. J., Fillingim, M. O., & Brain, D. A. (2011). Three-dimensional structure of the Martian nightside ionosphere: Predicted rates of impact ionization from Mars Global Surveyor magnetometer and electron reflectometer measurements of precipitating electrons. *Journal of Geophysical Research*, *116*, A12317. https://doi.org/10.1029/2011JA016982

Lillis, R. J., Fillingim, M. O., Peticolas, L. M., Brain, D. A., Lin, R. P., & Bougher, S. W. (2009). Nightside ionosphere of Mars: Modeling the effects of crustal magnetic fields and electron pitch angle distributions on electron impact ionization. *Journal of Geophysical Research*, *114*, E11009. https://doi.org/10.1029/2009JE003379

Lillis, R. J., Frey, H. V., & Manga, M. (2008). Rapid decrease in Martian crustal magnetization in the Noachian era: Implications for the dynamo and climate of early Mars. *Geophysical Research Letters*, *35*, L14203. https://doi.org/10.1029/2008GL034338

Lillis, R. J., Frey, H. V., Manga, M., Mitchell, D. L., Lin, R. P., Acuna, M. H., & Bougher, S. W. (2008). An improved crustal magnetic field map of Mars from electron reflectometry: Highland volcano magmatic history and the end of the martian dynamo. *Icarus*, *194*(2), 575–596. https://doi.org/10.1016/j.icarus.2007.09.032

Lillis, R. J., Lee, C. O., Larson, D. E., Luhmann, J., Halekas, J., Connerney, J., & Jakosky, B. (2016). Shadowing and anisotropy of solar energetic ions at Mars measured by MAVEN during the March 2015 solar storm. *Journal of Geophysical Research: Space Physics*, *121*, 2818–2829. https://doi.org/10.1002/2015JA022327

Lillis, R. J., Mitchell, D. L., Lin, R. P., & Acuna, M. H. (2008). Electron reflectometry in the martian atmosphere. *Icarus*, *194*(2), 544–561. https://doi.org/10.1016/j.icarus.2007.09.030

Lillis, R. J., Mitchell, D. L., Lin, R. P., Connerney, J. E. P., & Acuna, M. H. (2004). Mapping crustal magnetic fields at Mars using electron reflectometry. *Geophysical Research Letters*, *31*, L15702. https://doi.org/10.1029/2004GL020189

Lillis, R. J., Purucker, M. E., Halekas, J. S., Louzada, K. L., Stewart-Mukhopadhyay, S. T., Manga, M., & Frey, H. V. (2010). Study of impact demagnetization at Mars using Monte Carlo modeling and multiple altitude data. *Journal of Geophysical Research*, *115*, E07007. https://doi.org/10.1029/2009JE003556

Lillis, R. J., Robbins, S., Manga, M., Halekas, J. S., & Frey, H. V. (2013). Time history of the Martian dynamo from crater magnetic field analysis. *Journal of Geophysical Research: Planets*, *118*, 1488–1511. https://doi.org/10.1002/Jgre.20105

Lillis, R. J., Stewart, S. T., & Manga, M. (2013). Demagnetization by basin-forming impacts on early Mars: Contributions from shock, heat, and excavation. *Journal of Geophysical Research: Planets*, *118*, 1045–1062. https://doi.org/10.1002/Jgre.20085

Lundin, R., Winningham, D., Barabash, S., Frahm, R., Holmström, M., Sauvaud, J. A., … Wurz, P. (2006). Plasma acceleration above martian magnetic anomalies. *Science*, *311*(5763), 980–983. https://doi.org/10.1126/science.1122071

Lyons, L. R. (1980). Generation of large-scale regions of auroral currents, electric potentials, and precipitation by the divergence of the convection electric field. *Journal of Geophysical Research*, *85*, 17–24. https://doi.org/10.1029/JA085iA01p00017

Marklund, G., Johansson, T., Lileo, S., & Karlsson, T. (2007). Cluster observations of an auroral potential and associated field-aligned current reconfiguration during thinning of the plasma sheet boundary layer. *Journal of Geophysical Research*, *112*, A01208. https://doi.org/10.1029/2006JA011804

Mitchell, D. L., Lin, R. P., Mazelle, C., Rème, H., Cloutier, P. A., Connerney, J. E. P., … Ness, N. F. (2001). Probing Mars' crustal magnetic field and ionosphere with the MGS electron reflectometer. *Journal of Geophysical Research*, *106*, 23,419–23,427.

Mittelholz, A., Johnson, C. L., & Lillis, R. J. (2017). Global-scale external magnetic fields at Mars measured at satellite altitude. *Journal of Geophysical Research: Planets*, *122*, 1243–1257. https://doi.org/10.1002/2017JE005308

Morschhauser, A., Lesur, V., & Grott, M. (2014). A spherical harmonic model of the lithospheric magnetic field of Mars. *Journal of Geophysical Research: Planets*, *119*, 1162–1188. https://doi.org/10.1002/2013JE004555

Mozer, F. S., & Kletzing, C. A. (1998). Direct observation of large, quasi-static, parallel electric fields in the auroral acceleration region. *Geophysical Research Letters*, *25*, 1629–1632. https://doi.org/10.1029/98GL00849

Nagy, A. F., Winterhalter, D., Sauer, K., Cravens, T. E., Brecht, S., Mazelle, C., … Trotignon, J. G. (2004). The plasma environment of Mars. *Space Science Reviews*, *111*(1/2), 33–114. https://doi.org/10.1023/B:Spac.0000032718.47512.92

Opgenoorth, H. J., Dhillon, R. S., Rosenqvist, L., Lester, M., Edberg, N. J. T., Milan, S. E., … Brain, D. (2010). Day-side ionospheric conductivities at Mars. *Planetary and Space Science*, *58*(10), 1139–1151. https://doi.org/10.1016/j.pss.2010.04.004

Parks, G. K. (2004). *Physics of space plasmas* (p. 597). Oxford: Westview.

Press, W. H., Teukolsky, S. A., Vetterling, W. T., & Flannery, B. P. (1992). *Numerical recipes in C: the art of scientific computing*. Cambridge, UK: Cambridge University Press.

Riousset, J. A., Paty, C. S., Lillis, R. J., Fillingim, M. O., England, S. L., Withers, P. G., & Hale, J. P. M. (2013). Three-dimensional multifluid modeling of atmospheric electrodynamics in Mars' dynamo region. *Journal of Geophysical Research: Space Physics*, *118*, 3647–3659. https://doi.org/10.1002/Jgra.50328

Riousset, J. A., Paty, C. S., Lillis, R. J., Fillingim, M. O., England, S. L., Withers, P. G., & Hale, J. P. M. (2014). Electrodynamics of the Martian dynamo region near magnetic cusps and loops. *Geophysical Research Letters*, *41*, 1119–1125. https://doi.org/10.1002/2013GL059130

Robbins, S. J., Hynek, B. M., Lillis, R. J., & Bottke, W. F. (2013). Large impact crater histories of Mars: The effect of different model crater age techniques. *Icarus*, *225*(1), 173–184. https://doi.org/10.1016/j.icarus.2013.03.019

Ruhunusiri, S., Halekas, J. S., Espley, J. R., Mazelle, C., Brain, D., Harada, Y., … Howes, G. G. (2017). Characterization of turbulence in the Mars plasma environment with MAVEN observations. *Journal of Geophysical Research: Space Physics*, *122*, 656–674. https://doi.org/10.1002/2016JA023456

Ruhunusiri, S., Halekas, J. S., McFadden, J. P., Connerney, J. E. P., Espley, J. R., Harada, Y., … Hasegawa, H. (2016). MAVEN observations of partially developed Kelvin–Helmholtz vortices at Mars. *Geophysical Research Letters*, *43*, 4763–4773. https://doi.org/10.1002/2016GL068926

Schneider, N. M., Deighan, J. I., Jain, S. K., Stiepen, A., Stewart, A. I. F., Larson, D., … Jakosky, B. M. (2015). Discovery of diffuse aurora on Mars. *Science*, *350*(6261). https://doi.org/10.1126/science.aad0313

Thiemann, E. M. B., Chamberlin, P. C., Eparvier, F. G., Templeman, B., Woods, T. N., Bougher, S. W., & Jakosky, B. M. (2017). The MAVEN EUVM model of solar spectral irradiance variability at Mars: Algorithms and results. *Journal of Geophysical Research: Space Physics*, *122*, 2748–2767. https://doi.org/10.1002/2016JA023512

Xu, S., Liemohn, M. W., & Mitchell, D. L. (2014). Solar wind electron precipitation into the dayside Martian upper atmosphere through the cusps of strong crustal fields. *Journal of Geophysical Research: Space Physics*, *119*, 10,100–10,115. https://doi.org/10.1002/2014JA020363